Journal of Computational Physics 470 (2022) 111584

Contents lists available at ScienceDirect

Journal of Computational Physics

www.elsevier.com/locate/jcp

A direct sampling method for simultaneously recovering electromagnetic inhomogeneous inclusions of different nature

Yat Tin Chow [a], Fuqun Han [b], Jun Zou [b,*,1]

[a] Department of Mathematics, University of California, Riverside, United States of America
[b] Department of Mathematics, The Chinese University of Hong Kong, Shatin, N.T., Hong Kong

ARTICLE INFO

Article history:
Received 10 March 2022
Received in revised form 26 August 2022
Accepted 27 August 2022
Available online 5 September 2022

Keywords:
Inverse problem
Direct sampling method
Simultaneous reconstruction
Electromagnetic inclusions

ABSTRACT

In this work, we propose a novel direct sampling method (DSM) to recover the support of two different types of electromagnetic inhomogeneous inclusions simultaneously, with only one or two sets of noisy boundary measurement data. The DSM leverages upon an important mutually almost orthogonality property between the fundamental solutions of the forward problem and some proper families of probing functions. Two proper families of probing functions that possess desired properties are proposed to reconstruct the support of inhomogeneous inclusions accurately in the direction that is parallel to or vertical to the measurement surface separately. For the two families of probing functions, the mutually almost orthogonality property is carefully verified through both theoretical justifications and numerical experiments. The novel DSM is fast to compute, effective under limited measurement data, and very stable and robust against random noise of reasonable size. All these features are verified through extensive numerical experiments.

1. Introduction

We will propose a direct sampling method (DSM) to recover the support of electromagnetic inhomogeneous inclusions of different physical nature, i.e., the electric permittivity ϵ and the magnetic permeability μ in a physical media, where both unknown coefficients can be fully anisotropic in a time-harmonic Maxwell equation, with just one or two sets of noisy boundary measurements in $\mathbb{R}^3$.

The inverse problem is highly nonlinear, ill-posed and challenging numerically, and finds wide applications in various fields, including non-destructive testing [18], subsurface objects detection [22], earth surface mapping [30], and biomedical imaging [7]. In particular, the new DSM will be very useful for real scenarios when we are interested in both electric and magnetic properties of a physical domain, such as in reconstructing physical properties of metamaterials [1], detecting ferromagnetic minerals [22, Chapter 2], tracking synthetic nanoparticles with special electric and magnetic properties in complex biological environments [26], and the test for the hepatic iron overload in patients [29]. Moreover, since our method features its robustness and effectiveness under noisy and inadequate measurement data, the reconstruction from DSM can also serve as some fast, reliable, and reasonable initial estimates for computationally much more expensive optimization

* Corresponding author.
E-mail addresses: ytchow@ucr.edu (Y.T. Chow), fqhan@math.cuhk.edu.hk (F. Han), zou@math.cuhk.edu.hk (J. Zou).

[1] The work of this author was substantially supported by Hong Kong RGC grant (Projects 14306921 and 14306719).

https://doi.org/10.1016/j.jcp.2022.111584
0021-9991/

type methods or be applied to the cases where general qualitative information regarding inhomogeneous inclusions is required in a fast and stable manner.

As the inverse coefficient problem associated with the time harmonic Maxwell equation appears frequently in practical applications, many numerical methods have been proposed to solve this highly ill-posed non-linear inverse problem. In general, iterative methods that minimize an optimization functional with certain regularization are most popular which at the same time may be time consuming to solve and easily trapped by some local minima. In this case, many non-iterative methods are proposed to avoid the optimization process, for instance, linear sampling method [9], factorization type methods [23], multiple signal classification imaging method [3,33], methods using topological derivative [27], and reverse time migration [12]. For an in-depth introduction to non-iterative numerical methods for recovering electromagnetic inhomogeneous inclusions, we refer to recent monographs [10,13]. All these methods are applicable only for recovering inhomogeneous media of a single physical nature. To our knowledge, there are still no sampling type numerical methods in the literature that apply for more practical and challenging cases of recovering inhomogeneous inclusions of different physical nature simultaneously, which is the main focus of this work. There are some existing numerical methods for recovering two different types of electromagnetic inhomogeneous inclusions simultaneously, but these are mostly traditional type iterative methods for minimizing a large optimization functional with certain regularization [6,32], which are computationally very demanding and expensive and also require good and quantitative initial starting values (both geometric shapes and physical properties) of unknown inhomogeneous inclusions. These traditional type methods are essentially different from our direct sampling type methods to be developed in this work.

In this paper, motivated by the previous direct sampling type methods for wave and non-wave type inverse problems developed for recovering inhomogeneous media of a single physical nature, see, e.g., [15–17,20,21,24,28], we propose a novel DSM for more practical and challenging cases of recovering inhomogeneous inclusions of different physical nature simultaneously [14], while it still preserves the features of the existing direct sampling type methods, i.e., easy to implement, fast to compute, highly parallelable, and robust under noisy and limited measurement data. In order to be able to identify the support of inhomogeneous inclusions associated with different types of anisotropic coefficients, we will construct two new families of probing functions, and each family consists of two sets of probing functions that only interact well with the signal that comes from electric or magnetic inhomogeneous inclusions separately. The crucial property associated with probing functions is called the mutually almost orthogonality property, which will be described explicitly in the next section and verified. This crucial property allows the new DSM to be able to identify both the support of inhomogeneous inclusions and their physical features.

Following the above mentioned general idea of direct sampling type methods, we construct and investigate two families of probing functions for a representative measurement surface, i.e., the unit sphere. The construction of the first family is based on our unique observation that the sharpness of index functions can be improved through a surface Laplacian. Our investigation on the corresponding imaging kernel functions with this new family of probing functions shows a significant improvement of the accuracy in recovering the support of inhomogeneous inclusions distributed in the direction that is parallel to the measurement surface. On the other hand, in order to improve the accuracy of the reconstruction in the radial direction, i.e., the direction that is vertical to the measurement surface, we construct the probing functions such that their corresponding kernel functions approximate Gaussian kernels in the radial direction. For both of the two families of probing functions, the desired mutually almost orthogonality property is carefully verified.

The remaining of the paper is organized as follows. In section 2, with an introduction for the inverse problem under consideration, we discuss the motivation and general formulation of direct sampling type methods. In section 3, assuming the incident field is known, we propose two families of probing functions that possess the mutually almost orthogonality property and can generate quite satisfactory reconstruction results in the direction that is parallel to or vertical to the measurement surface separately. The desired mutually almost orthogonal property is investigated in detail through theoretical justifications and numerical experiments. In section 4, we further consider the inverse problem of recovering the support of inhomogeneous inclusions from the measurement data for both the electric and magnetic field on the boundary, with no prior knowledge of the incident field. The design and analysis of the corresponding DSM are very similar to section 3, hence we highlight the difference and provide key steps for this scenario in constructing suitable index functions. In section 5, a set of numerical experiments are conducted to verify the accuracy, robustness, and stability of the proposed DSM under measurement data with reasonably large noise.

We end this section with an introduction to some frequently used notation in the following sections. $\Re a$ and $\Im a$ represent the real and imaginary parts of a complex number a, and $\mathbb{S}^2$ and $B(0,1)$ are the unit sphere and unit ball in $\mathbb{R}^3$. $j_n(x)$ and $h_n^{(1)}$ are the spherical Bessel function of the first kind and the spherical Hankel function of the first kind of order n, and $P_n^m(t)$ denotes the associated Legendre polynomial of order (n,m).

2. General principles of direct sampling type methods

In this section, we consider an inverse electromagnetic scattering problem, where the electromagnetic field is induced by a known incident field E^i, and study the more practical and challenging case that the incident field is unknown in section 4. Consider the time-harmonic electric field system

$$\nabla \times (\frac{1}{\mu}\nabla \times E) - k^2 \epsilon E = 0 \quad \text{in } \mathbb{R}^3, \tag{2.1}$$

where k is a fixed wavenumber, and ϵ and μ are the electric permittivity and magnetic permeability of the physical media, which we aim to recover. We allow the medium to be anisotropic, namely,

$$\epsilon = \mathrm{diag}(\varepsilon_1, \varepsilon_2, \varepsilon_3), \quad \mu = \mathrm{diag}(\mu_1, \mu_2, \mu_3)\,, \tag{2.2}$$

where $\Re\{\epsilon_i\}$ and $\Re\{\mu_i\}$ are positive for $i = 1, 2, 3$. Letting E^i and $E^s := E - E^i$ be the incident and scattered fields, then E^i satisfies a similar equation to (2.1), while E^s is imposed to meet the standard radiation condition:

$$\nabla \times ({\mu_0}^{-1} \nabla \times E^i) - k^2 \epsilon_0 E^i = 0 \quad \text{in } \mathbb{R}^3\,, \tag{2.3}$$

$$\lim_{r_x \to \infty} r_x (\nabla \times E^s \times \hat{x} - ikE^s) = 0\,, \tag{2.4}$$

where $r_x = |x|$ and $\hat{x} = x/r_x$ for any $x \in \mathbb{R}^3$, and ϵ_0 and μ_0 are the coefficients of the homogeneous background.

Consider a bounded domain Ω in $\mathbb{R}^3$ with a $C^{1,1}$ boundary, on which one or two sets of data of $\nu \times E$ is measured associated with one frequency k. Assume there are some inhomogeneous inclusions of different physical nature lying in Ω, induced from the electric permittivity and magnetic permeability, respectively, i.e.,

$$\Omega_\mu := \mathrm{supp}\{\mu - \mu_0\} \subset \Omega\,, \quad \Omega_\epsilon := \mathrm{supp}\{\epsilon - \epsilon_0\} \subset \Omega\,. \tag{2.5}$$

The main objective of this work is to construct a DSM to recover all these inhomogeneous inclusions of different physical nature simultaneously.

The primary motivation of direct sampling type methods is the approximate orthogonality property between fundamental solutions of the forward problem and properly chosen families of probing functions in some dual products. We now recall the free space Green's function Φ_x for the Maxwell equation, satisfying

$$\nabla \times \nabla \times \Phi_x(y) - k^2 \Phi_x(y) = \delta_x(y) \boldsymbol{I}_3\,, \quad \nabla_y \cdot \Phi_x(y) = 0\,, \tag{2.6}$$

and radiation condition (2.4). For any $\boldsymbol{p}_0 \in \mathbb{C}^3$, we can represent Φ_x as

$$\Phi_x \cdot \boldsymbol{p}_0 = (G_x \boldsymbol{p}_0) + \frac{1}{k^2} \nabla \nabla \cdot (G_x \boldsymbol{p}_0)\,, \quad \nabla \times (\Phi_x \cdot \boldsymbol{p}_0) = \nabla \times (G_x \boldsymbol{p}_0)\,, \tag{2.7}$$

where G_x is the Green's function for the Helmholtz equation:

$$G_x(y) := \frac{1}{4\pi} \frac{e^{ik|y-x|}}{|y-x|}\,. \tag{2.8}$$

In order to design a direct sampling type method, we would like to represent the boundary measurement, i.e., $\nu \times E^s$, with a discrete sum of the fundamental solutions of the forward problem. Hence, we first substitute $E^s = E - E^i$ and (2.3) into (2.1) to derive

$$\nabla \times \nabla \times E^s - k^2 E^s = -\nabla \times \Big[\Big(\frac{1}{\mu} - \frac{1}{\mu_0} \Big) \nabla \times E \Big] + k^2 (\epsilon - \epsilon_0) E\,. \tag{2.9}$$

Then with an application of the Green's representation formula, we have

$$E^s(x) = -\int_\Omega \Phi_x \Big\{ \nabla \times \Big[\big(\frac{1}{\mu} - \frac{1}{\mu_0} \big) \nabla \times E \Big] - k^2 (\epsilon - \epsilon_0) E \Big\} dy\,. \tag{2.10}$$

For the case that μ is a smooth function, E^s can be written as

$$E^s(x) = \int_{\Omega_\epsilon} k^2 (\epsilon - \epsilon_0) \Phi_x E dy - \int_{\Omega_\mu} \Big(\frac{1}{\mu} - \frac{1}{\mu_0} \Big) (\nabla \times \Phi_x)(\nabla \times E) dy\,; \tag{2.11}$$

and if μ is a piecewise constant, we may write E^s as

$$E^s(x) = \int_{\Omega_\epsilon} k^2 (\epsilon - \epsilon_0) \Phi_x E dy - \Big(\frac{1}{\mu} - \frac{1}{\mu_0} \Big) \Big(\int_{\Omega_\mu} (\nabla \times \Phi_x)(\nabla \times E) dy + \int_{\partial \Omega_\mu} (\nu \times \nabla \times \Phi_x) E ds_y \Big)\,. \tag{2.12}$$

For either case, we notice that the scattered field can be approximated by a linear combination of the Green's function $\Phi_x(y_i)$ and its curl $\nabla \times \Phi_x(z_j)$, namely, it holds for some $a_i, b_j \in \mathbb{C}$ and $\boldsymbol{c}_i, \boldsymbol{d}_j \in \mathbb{C}^3$ that

$$E^s(x) \approx \sum_i a_i (\Phi_x(y_i) \cdot \boldsymbol{c}_i) + \sum_j b_j \nabla \times (\Phi_x(z_j) \cdot \boldsymbol{d}_j)\,, \quad x \in \partial\Omega\,,\ y_i \in \Omega_\epsilon\,,\ z_j \in \Omega_\mu\,. \tag{2.13}$$

In the sequel, we will call Φ_{y_i} and $\nabla \times \Phi_{z_j}$ the electric monopole and magnetic monopole, respectively.

As we will see, the new direct sampling type method reconstructs the inhomogeneous media Ω_ϵ and Ω_μ by means of two index functions:

$$I_{mo}(z) = \frac{\langle \nu \times E^s,\ \boldsymbol{w}_z^1 \cdot \boldsymbol{p}_z \rangle_{L^2(\partial\Omega)}}{n(z)}, \quad I_{di}(z) = \frac{\langle \nu \times E^s,\ \boldsymbol{w}_z^2 \cdot \boldsymbol{q}_z \rangle_{L^2(\partial\Omega)}}{n(z)}, \quad \forall z \in \Omega, \tag{2.14}$$

which are formed basically by the measurement data and two probing functions $\boldsymbol{w}_z^1$ and $\boldsymbol{w}_z^2$. In (2.14), $\boldsymbol{p}_z$, $\boldsymbol{q}_z \in \mathbb{C}^3$ are two probing directions to be determined, and $n(z)$ is some normalization. We know the magnetic monopole associated with $\nabla \times \Phi_x$ can be considered as an analog of the electric dipole, which will be used in the second index function above. This is why we add the subscript "di" there. We would like to remark that, as we see from (2.14), the evaluation of the index functions mainly involves the inner products between the measurement data and the probing functions associated with the sampling point z. Hence, the index functions at all sampling points are able to evaluate completely independently of each other and the resulting direct sampling method is therefore implementable fully in parallel.

We now illustrate the basic principle for the above index functions to reconstruct inhomogeneous inclusions. For this, we define four kernel functions:

$$K^1_{\boldsymbol{c}_x,\boldsymbol{p}_z}(x,z) = \frac{\langle \nu \times (\Phi_x^1 \cdot \boldsymbol{c}_x),\ \boldsymbol{w}_z^1 \cdot \boldsymbol{p}_z \rangle_{L^2(\partial\Omega)}}{n(z)}, \qquad K^2_{\boldsymbol{d}_x,\boldsymbol{p}_z}(x,z) = \frac{\langle \nu \times (\nabla \times \Phi_x^2 \cdot \boldsymbol{d}_x),\ \boldsymbol{w}_z^1 \cdot \boldsymbol{p}_z \rangle_{L^2(\partial\Omega)}}{n(z)}; \tag{2.15}$$

$$K^3_{\boldsymbol{c}_x,\boldsymbol{q}_z}(x,z) = \frac{\langle \nu \times (\Phi_x^1 \cdot \boldsymbol{c}_x),\ \boldsymbol{w}_z^2 \cdot \boldsymbol{q}_z \rangle_{L^2(\partial\Omega)}}{n(z)}, \qquad K^4_{\boldsymbol{d}_x,\boldsymbol{q}_z}(x,z) = \frac{\langle \nu \times (\nabla \times \Phi_x^2 \cdot \boldsymbol{d}_x),\ \boldsymbol{w}_z^2 \cdot \boldsymbol{q}_z \rangle_{L^2(\partial\Omega)}}{n(z)}. \tag{2.16}$$

With these kernel functions and the approximation (2.13), we can rewrite the index functions approximately:

$$I_{mo}(x) \approx \sum_i a_i K^1_{\boldsymbol{c}_x,\boldsymbol{p}_{y_i}}(x,y_i) + \sum_j b_j K^2_{\boldsymbol{d}_x,\boldsymbol{p}_{z_j}}(x,z_j), \tag{2.17}$$

$$I_{di}(x) \approx \sum_i a_i K^3_{\boldsymbol{c}_x,\boldsymbol{q}_{y_i}}(x,y_i) + \sum_j b_j K^4_{\boldsymbol{d}_x,\boldsymbol{q}_{z_j}}(x,z_j). \tag{2.18}$$

Then the following mutually almost orthogonality property will be crucial to our numerical reconstruction.

Mutually almost orthogonality property (MAOP):

- The magnitude of $K^1_{\boldsymbol{c}_x,\boldsymbol{p}_z}(x,z)$ and $K^4_{\boldsymbol{d}_x,\boldsymbol{q}_z}(x,z)$ reach a maximum at $z = x$ under a proper choice of probing directions $\boldsymbol{p}_z$ and $\boldsymbol{q}_z$;
- The magnitude of $K^2_{\boldsymbol{d}_x,\boldsymbol{p}_z}(x,z)$ and $K^3_{\boldsymbol{c}_x,\boldsymbol{q}_z}(x,z)$ are small compared with that of $K^1_{\boldsymbol{c}_x,\boldsymbol{p}_z}(x,z)$ and $K^4_{\boldsymbol{d}_x,\boldsymbol{q}_z}(x,z)$ for any x, z under any choices of probing directions $\boldsymbol{p}_z$ and $\boldsymbol{q}_z$.

We can also restate the above property as follows: when x is close to z, the first set of probing functions $\boldsymbol{w}_z^1$ interact well with Φ_x while the second set of probing functions $\boldsymbol{w}_z^2$ interact strongly with $\nabla \times \Phi_x$. However, the interactions between $\boldsymbol{w}_z^1$ and $\nabla \times \Phi_x$ and between $\boldsymbol{w}_z^2$ and Φ_x are relatively weak for any choices of x and z. Therefore, the index $I_{mo}(z)$ will be relatively large only when $z \in \Omega_\epsilon$ while $I_{di}(z)$ will be relatively large only when $z \in \Omega_\mu$. These behaviors are used to help locate inhomogeneous inclusions and identify their physical properties. Moreover, the resolution and the accuracy of the reconstruction can be improved if the kernel functions are sharper in the sense that $\left|K^1_{\boldsymbol{c}_x,\boldsymbol{p}_z}(x,z)\right|$ and $\left|K^4_{\boldsymbol{d}_x,\boldsymbol{q}_z}(x,z)\right|$ decay faster for z along any direction that points away from x. This motivates us to mainly investigate the properties of the kernel functions corresponding to some special choices of probing functions in section 3.

Under the settings above, two index functions in (2.14) give rise to our **direct sampling method** (DSM):

Given the measurement data $\nu \times E^s$ on $\partial\Omega$, and a set of discrete sampling points $z \in \Omega$,
(i) evaluate $I_{\rm mo}$ to recover the electric permittivity inclusions, i.e., supp$(\epsilon - \epsilon_0)$;
(ii) evaluate $I_{\rm di}$ to recover the magnetic permeability inclusions, i.e., supp$\{\mu - \mu_0\}$.

Before we proceed to explicitly define probing functions, we would like to remark that for the reconstruction of the anisotropic medium, especially for the common case that ϵ and μ are symmetric matrices, we can write

$$\epsilon = Q^* D Q, \quad D = \mathrm{diag}(\varepsilon_1, \varepsilon_2, \varepsilon_2),$$
$$\mu = \tilde{Q}^* \tilde{D} \tilde{Q}, \quad \tilde{D} = \mathrm{diag}(\mu_1, \mu_2, \mu_2)$$

where Q and $\tilde{Q}$ are two unitary matrices. Then the almost orthogonality property that we shall rely on to reconstruct ϵ and μ is still valid, by using the above diagonalizations of ϵ and μ and following the basic analyzes in the subsequent sections with some technical modifications. However, for the sake of presentation, we mainly focus on the cases that ϵ and μ are scalar or diagonal matrices in this work, while the method is indeed applicable to more general cases which will be demonstrated in example 3 of section 5.

3. Probing functions and verification of the mutually almost orthogonality property

In this section, we construct some appropriate families of probing functions for us to use in recovering the support of inhomogeneous inclusions of different nature via the index functions proposed in (2.14). Based on the general principles for direct sampling type methods we introduced in section 2, we verify the desired mutually almost orthogonality property for two new families of probing functions, and for the most representative measurement surface in real applications, i.e., $\partial\Omega = \mathbb{S}^2$ and $\Omega = B(0,1)$ where $B(0,1)$ is the unit ball.

We start with a brief overview of the arrangements in the subsequent subsections.

- Two sets of probing functions are introduced in section 3.1, and the mutually almost orthogonality property is verified.
- To improve the reconstruction accuracy in the direction that is parallel to the measurement surface, we apply in section 3.2 the spherical Laplacian to the probing functions and then make necessary modifications to enhance numerical stability. The proposed strategy is carefully verified with the help of spherical vector waves through both theoretical justification and numerical experiments.
- To improve the reconstruction accuracy in the direction that is vertical to the measurement surface, i.e., the radial direction, we construct in section 3.3 the probing functions such that the resulting kernel functions approximate a Gaussian kernel in the radial direction with a relatively small error. The corresponding mutually almost orthogonality property is justified.

We remark that the families of probing functions to be constructed in sections 3.2 and 3.3 can be used either independently or simultaneously for more desirable reconstruction results in applications.

3.1. A family of probing functions motivated by back-propagation

In this subsection, we construct probing functions that are directly motivated by the idea of back-propagation, that is, using the imaginary part of the Green's function as the kernel function. This family of probing functions will be a reasonable candidate for our DSM when the wavenumber k is relatively large, and also provide a convenient starting point for our upcoming construction of other probing functions that can generate more accurate reconstruction results.

Let us consider a typical and frequently used measurement surface $\partial\Omega = \mathbb{S}^2$. We will use the completeness and orthogonality of the spherical vector waves (see $\boldsymbol{v}_{\tau,m,n}$ and $\boldsymbol{u}_{\tau,m,n}$ defined in (A.5) and (A.7) in Appendix A, where the definitions and some important properties are also given).

We first recall the representation of the free space Green's function (cf. (2.6)) by spherical vector waves [31]:

$$\Phi_x(y) = ik \sum_{-n\le m\le n,\, n\in\mathbb{N}} \Big[\boldsymbol{v}_{1,m,n}(x)\boldsymbol{u}^{\dagger}_{1,m,n}(y) + \boldsymbol{v}_{2,m,n}(x)\boldsymbol{u}^{\dagger}_{2,m,n}(y) \Big], \quad r_y > r_x\,, \tag{3.1}$$

where and in the sequel, $\boldsymbol{v}^{\dagger}_{\tau,m,n}$ and $\boldsymbol{u}^{\dagger}_{\tau,m,n}$ are the vector functions obtained by replacing all spherical harmonics Y_n^m in the definitions of spherical vector waves (see (A.5), (A.7)) by their complex conjugate and then taking the non-conjugate transpose. For the notational sake, we shall write $\sum_{-n\le m\le n,\, n\in\mathbb{N}}$ simply as $\sum_{m,n}$ below.

We can rewrite the curl of Φ_x in the formula (3.2) below by using (3.1), while the imaginary part of Φ_x can be represented similarly (Lemma 3.1 below, whose proof follows from section 10-2 of [31], with radiating spherical vector waves replaced by regular spherical vector waves):

$$\nabla\times\Phi_x(y) = ik^2 \sum_{m,\,n} \Big[\boldsymbol{v}_{2,m,n}(x)\boldsymbol{u}^{\dagger}_{1,m,n}(y) + \boldsymbol{v}_{1,m,n}(x)\boldsymbol{u}^{\dagger}_{2,m,n}(y) \Big]. \tag{3.2}$$

Lemma 3.1. *For any x, $y \in \mathbb{R}^3$, we have*

$$\Im\{\Phi_x(y)\} = ik \sum_{m,\,n} \Big[\boldsymbol{v}_{1,m,n}(x)\boldsymbol{v}^{\dagger}_{1,m,n}(y) + \boldsymbol{v}_{2,m,n}(x)\boldsymbol{v}^{\dagger}_{2,m,n}(y) \Big]. \tag{3.3}$$

It is well-known that $\Im\{\Phi_x(z)\}$ is used in the time reversal imaging [19] to recover the support of inhomogeneous inclusions. This motivates us to design two sets of probing functions $\boldsymbol{w}_z^1$ and $\boldsymbol{w}_z^2$ such that the kernel functions (cf. (2.15))-(2.16)) are the imagery part of the free space Green's function and its curl separately. Using this idea, the representation (3.1) and the orthogonality of spherical vector waves (cf. (A.10)), we propose to construct a family of probing functions $\boldsymbol{w}_z(y)$ by expressing the interaction between $\boldsymbol{w}_z$ and Φ_x in the form:

$$\begin{aligned} \langle \nu\times(\Phi_x\cdot\boldsymbol{c}_x),\ \boldsymbol{w}_z\rangle_{L^2(\partial\Omega)} = \sum_{m,n} \Big[&\big\langle \nu\times\boldsymbol{u}^{\dagger}_{1,m,n},\ a_{2,m,n}(z)\boldsymbol{u}^{\dagger}_{2,m,n} + a_{3,m,n}(z)\boldsymbol{u}^{\dagger}_{3,m,n}\big\rangle_{L^2(\partial\Omega)} \boldsymbol{v}_{1,m,n}(x)\cdot\boldsymbol{c}_x \\ &+ \big\langle \nu\times\boldsymbol{u}^{\dagger}_{2,m,n},\ a_{1,m,n}(z)\boldsymbol{u}^{\dagger}_{1,m,n} + a_{4,m,n}(z)\boldsymbol{u}^{\dagger}_{4,m,n}\big\rangle_{L^2(\partial\Omega)} \boldsymbol{v}_{2,m,n}(x)\cdot\boldsymbol{c}_x \Big] \end{aligned} \tag{3.4}$$

for any $\boldsymbol{c}_x \in \mathbb{C}^3$, where the choices of coefficients $a_{\tau,m,n}$ in (3.4) are totally free. Then for any function $K(x,z)$, e.g., a function that admits an expansion $K(x,z) = \sum_{\substack{\tau=1,2\\ m,n}} b_{\tau,m,n}(z)\boldsymbol{v}_{\tau,m,n}(x)$, we may find a corresponding probing function $\boldsymbol{w}_z$ of the form $\boldsymbol{w}_z(y) := \sum_{\substack{\tau=1,2,3,4,\\ m,n}} a_{\tau,m,n}(z)\boldsymbol{u}^{\dagger}_{\tau,m,n}(y)$ such that

$$\langle \nu \times (\Phi_x \cdot \boldsymbol{c}_x),\ \boldsymbol{w}_z\rangle_{L^2(\partial\Omega)} = K(x,z)\cdot \boldsymbol{c}_x\,.$$

Indeed we can determine $a_{\tau,m,n}$ by solving (comparing the coefficients between (3.4) and $K(x,z)$)

$$b_{1,m,n}(z) = \langle \nu \times \boldsymbol{u}^{\dagger}_{1,m,n},\ a_{2,m,n}(z)\boldsymbol{u}^{\dagger}_{2,m,n} + a_{3,m,n}(z)\boldsymbol{u}^{\dagger}_{3,m,n}\rangle_{L^2(\partial\Omega)}\,, \tag{3.5}$$

$$b_{2,m,n}(z) = \langle \nu \times \boldsymbol{u}^{\dagger}_{2,m,n},\ a_{1,m,n}(z)\boldsymbol{u}^{\dagger}_{1,m,n} + a_{4,m,n}(z)\boldsymbol{u}^{\dagger}_{4,m,n}\rangle_{L^2(\partial\Omega)} \tag{3.6}$$

for all $-n \le m \le n$, $n \in \mathbb{N}$. Using this process, by choosing $b_{1,m,n}(z) = \boldsymbol{v}^{\dagger}_{1,m,n}(z)$, $b_{2,m,n}(z) = \boldsymbol{v}^{\dagger}_{2,m,n}(z)$ in (3.5), we can readily obtain two sets of probing functions $\boldsymbol{w}^{1,0}_z$ and $\boldsymbol{w}^{2,0}_z$ for $z \in \Omega$ and $y \in \partial\Omega$:

$$\boldsymbol{w}^{1,0}_z(y) := \sum_{m,n}\Big[\boldsymbol{v}_{2,m,n}(z)(\boldsymbol{u}^{\dagger}_{1,m,n}(y) + c_{4,n}\boldsymbol{u}^{\dagger}_{4,m,n}(y)) + \boldsymbol{v}_{1,m,n}(z)(\boldsymbol{u}^{\dagger}_{2,m,n}(y) + c_{3,n}\boldsymbol{u}^{\dagger}_{3,m,n}(y))\Big]\,, \tag{3.7}$$

$$\boldsymbol{w}^{2,0}_z(y) := \frac{1}{k}\sum_{m,n}\Big[\boldsymbol{v}_{1,m,n}(z)(\boldsymbol{u}^{\dagger}_{1,m,n}(y) + c_{4,n}\boldsymbol{u}^{\dagger}_{4,m,n}(y)) + \boldsymbol{v}_{2,m,n}(z)(\boldsymbol{u}^{\dagger}_{2,m,n}(y) + c_{3,n}\boldsymbol{u}^{\dagger}_{3,m,n}(y))\Big]\,, \tag{3.8}$$

where $c_{3,n} = (-c_{n,1,2}+1)/\overline{c_{n,1,3}}$ and $c_{4,n} = (\overline{c_{n,1,2}}+1)/\overline{c_{n,2,4}}$, with $c_{n,i,j}$ from (A.10). This leads to the explicit representations of the kernel functions as introduced in (2.15):

$$K^{1,0}_{\boldsymbol{c}_x,\boldsymbol{p}_z}(x,z) = \langle \nu \times (\Phi_x \cdot \boldsymbol{c}_x),\ \boldsymbol{w}^{1,0}_z \cdot \boldsymbol{p}_z\rangle_{L^2(\partial\Omega)} = \sum_{\substack{\tau=1,2,\\ m,n}} \boldsymbol{v}_{\tau,m,n}(x)\boldsymbol{v}^{\dagger}_{\tau,m,n}(z) = \boldsymbol{c}_x^T\Im\{\Phi_x(z)\}\boldsymbol{p}_z\,, \tag{3.9}$$

$$K^{2,0}_{\boldsymbol{d}_x,\boldsymbol{p}_z}(x,z) = \langle \nu \times (\nabla\times\Phi_x \cdot \boldsymbol{d}_x),\ \boldsymbol{w}^{1,0}_z \cdot \boldsymbol{p}_z\rangle_{L^2(\partial\Omega)} = k\sum_{\substack{\tau=1,2,\\ m,n}} \boldsymbol{v}_{\tau,m,n}(x)\boldsymbol{v}^{\dagger}_{\tau,m,n}(z) = k\boldsymbol{d}_x^T\nabla\times\Im\{\Phi_x(z)\}\boldsymbol{p}_z\,, \tag{3.10}$$

$$K^{3,0}_{\boldsymbol{c}_x,\boldsymbol{q}_z}(x,z) = \langle \nu \times (\Phi_x \cdot \boldsymbol{c}_x),\ \boldsymbol{w}^{2,0}_z \cdot \boldsymbol{q}_z\rangle_{L^2(\partial\Omega)} = \frac{1}{k}\sum_{\substack{\tau=1,2,\\ m,n}} \boldsymbol{v}_{\tau,m,n}(x)\boldsymbol{v}^{\dagger}_{\tau,m,n}(z) = \frac{1}{k}\boldsymbol{c}_x^T\nabla\times\Im\{\Phi_x(z)\}\boldsymbol{q}_z\,, \tag{3.11}$$

$$K^{4,0}_{\boldsymbol{d}_x,\boldsymbol{q}_z}(x,z) = \langle \nu \times (\nabla\times\Phi_x \cdot \boldsymbol{d}_x),\ \boldsymbol{w}^{2,0}_z \cdot \boldsymbol{q}_z\rangle_{L^2(\partial\Omega)} = \sum_{\substack{\tau=1,2,\\ m,n}} \boldsymbol{v}_{\tau,m,n}(x)\boldsymbol{v}^{\dagger}_{\tau,m,n}(z) = \boldsymbol{d}_x^T\Im\{\Phi_x(z)\}\boldsymbol{q}_z\,, \tag{3.12}$$

where the 0's that appeared in the superscripts are used to distinguish different families of probing functions to be introduced. Hence, the index functions in (2.14) become (without the normalization term)

$$I^0_{mo}(z) = \langle \nu \times E^s,\ \boldsymbol{w}^{1,0}_z \cdot \boldsymbol{p}_z\rangle_{L^2(\partial\Omega)}\,,\quad I^0_{di}(z) = \langle \nu \times E^s,\ \boldsymbol{w}^{2,0}_z \cdot \boldsymbol{q}_z\rangle_{L^2(\partial\Omega)}\,. \tag{3.13}$$

We observe from (3.9)-(3.12) that the expressions of $K^{1,0}_{\boldsymbol{c}_x,\boldsymbol{p}_z}(x,z)$ and $K^{4,0}_{\boldsymbol{c}_x,\boldsymbol{p}_z}(x,z)$ are the same, so are the expressions of $K^{2,0}_{\boldsymbol{d}_x,\boldsymbol{p}_z}(x,z)$ and $k^2K^{3,0}_{\boldsymbol{d}_x,\boldsymbol{p}_z}(x,z)$. This will simplify our subsequent verification of the mutually almost orthogonality property of kernel functions.

Verification of the mutually almost orthogonality property. Using (3.9)-(3.12), it suffices to verify if the pair of the imaginary part of the Green's function and its curl possesses the desired mutually almost orthogonality property, namely, if the magnitude of $\boldsymbol{c}_x^T\Im\{\Phi_x(z)\}\boldsymbol{p}_z$ reaches the maximum when $x \approx z$, $\boldsymbol{c}_x \approx \boldsymbol{p}_z$, and if the magnitude of $\boldsymbol{c}_x^T\Im\{\nabla_z\times\Phi_x(z)\}\boldsymbol{q}_z$ is small for any choices of x and z. From (2.7), we have

$$\begin{aligned}\Im\{\Phi_x(z)\} =& \frac{k|x-z|\cos(k|x-z|) + (k^2|x-z|^2-1)\sin(k|x-z|)}{|x-z|^3}\boldsymbol{I}_3\\ &- \frac{3k|x-z|\cos(k|x-z|) + (k^2|x-z|^2-3)\sin(k|x-z|)}{|x-z|^3}D(x,z)\,;\end{aligned} \tag{3.14}$$

$$\Im\{\nabla\times\Phi_x(z)\} = \Big[\nabla_z\times\Big(\frac{\sin(k|x-z|)}{|x-z|}\boldsymbol{I}_3\Big)\Big] = \begin{pmatrix} 0 & -\frac{\partial}{\partial z_3} & \frac{\partial}{\partial z_2}\\ \frac{\partial}{\partial z_3} & 0 & -\frac{\partial}{\partial z_1}\\ -\frac{\partial}{\partial z_2} & \frac{\partial}{\partial z_1} & 0\end{pmatrix}\Big(\frac{\sin(k|x-z|)}{|x-z|}\boldsymbol{I}_3\Big)\,,$$

where $d_i = (x-z)_i$, $D(x,z) = (d_1,d_2,d_3)^T(d_1,d_2,d_3)/|x-z|^2$ and $\boldsymbol{I}_3$ is the 3×3 identity matrix.

Now we examine the ij-entry of $\Im\{\Phi_x(z)\}$ and $\Im\{\nabla\times\Phi_x(z)\}$ for $i,j=1,2,3$ when $x\approx z$. Applying the small angle approximation to trigonometric functions up to the order $\mathcal{O}(|x-z|^4)$, we derive

$$(\Im\{\Phi_x(z)\})_{i,j} = \delta_{i,j}\Big[-\frac{2k^5|x-z|^2}{15}+\frac{2k^3}{3}\Big]-\frac{d_id_j}{|x-z|^2}\Big(\frac{k^7|x-z|^4}{120}-\frac{k^5|x-z|^2}{15}\Big)+\mathcal{O}(|x-z|^4)\,, \tag{3.15}$$

$$|(\Im\{\nabla\times\Phi_x(z)\})_{i,j}| = \Big|\Big(\frac{k^3}{3}-\frac{k^5|x-z|^2}{30}\Big)(d_i-d_j)\Big|+\mathcal{O}(|x-z|^4)\,. \tag{3.16}$$

To be more precise on the assumption $\boldsymbol{c}_x\approx\boldsymbol{p}_z$, we consider a quite general scenario that $(\boldsymbol{c}_x)_i=\alpha_i(\boldsymbol{p})_i$ for some $\alpha_i\geq 0$. From the above two expansions, we observe the following:

- For $K^{1,0}_{\boldsymbol{c}_x,\boldsymbol{p}_z}(x,z)=\boldsymbol{c}_x^T\Im\{\Phi_x(z)\}\boldsymbol{p}_z$ defined in (3.9), it follows from (3.15) that

$$\boldsymbol{c}_x^T\Im\{\Phi_x(z)\})\boldsymbol{p}_z = 2k^3\boldsymbol{c}_x^T\boldsymbol{p}_z-\frac{2k^5}{5}\Big(\boldsymbol{c}_x^T\boldsymbol{p}_z-\frac{1}{6}\boldsymbol{c}_x^TD(x,z)\boldsymbol{p}_z\Big)|x-z|^2+\mathcal{O}(|x-z|^4)\,.$$

  By the assumption on $\boldsymbol{c}_x$ and $\boldsymbol{p}_z$, and noting that every entry of $D(x,z)$ is bounded by 1, we have $\boldsymbol{c}_x^T\boldsymbol{p}_z\geq 0$ and $\boldsymbol{c}_x^T\boldsymbol{p}_z-\frac{1}{6}\boldsymbol{c}_x^TD(x,z)\boldsymbol{p}_z\geq 0$. Then $K^{1,0}_{\boldsymbol{c}_x,\boldsymbol{p}_z}(x,z)$ is a quadratic polynomial with respect to $|x-z|$ and the only maximum point is at $x=z$, up to a small term $\mathcal{O}(|x-z|^4)$. This verifies the first part of the mutually almost orthogonality property that we proposed at the end of section 2.
- When $|x-z|\to 0$, we have from (3.15)-(3.16) that $(\Im\{\Phi_x(z)\})_{i,i}=2k^3/3+\mathcal{O}(|x-z|^2)$ and $|(\Im\{\nabla\times\Phi_x(z)\})_{i,j}|\leq 2|x-z|k^3/3+\mathcal{O}(|x-z|^2)$ $(i,j=1,2,3)$, respectively. Hence, the magnitude of the kernel function $K^{1,0}_{\boldsymbol{c}_x,\boldsymbol{p}_z}(x,z)$ is much larger than $K^{2,0}_{\boldsymbol{d}_x,\boldsymbol{p}_z}(x,z)$ when x and z are close enough for any possible choices of direction $\boldsymbol{d}_x$ associated with point x. This verifies the second part of the mutually almost orthogonality property.

Although the probing functions in (3.7)-(3.8) possess our desired mutually almost orthogonality property that helps locate inhomogeneous inclusions of different types, it is insufficient in some cases. To see this, we consider a special case of two electric monopoles locating at x and $-x$, with the direction $\boldsymbol{d}=(1,0,0)^T$, then

$$K^{1,0}_{\boldsymbol{d},\boldsymbol{d}}(x,z)+K^{1,0}_{\boldsymbol{d},\boldsymbol{d}}(-x,z)=\boldsymbol{d}^T[\Im\{\Phi_x(z)\}+\Im\{\Phi_{-x}(z)\}]\boldsymbol{d}=k^2\Big(\frac{\sin(k|x-z|)}{|x-z|}+\frac{\sin(k|(-x)-z|)}{|(-x)-z|}\Big)\,.$$

In order to separate two electric monopoles from the boundary measurement, we may require $2K^{1,0}_{\boldsymbol{d},\boldsymbol{d}}(x,0)<K^{1,0}_{\boldsymbol{d},\boldsymbol{d}}(x,x)$, i.e. two distinct maximum points can be observed at both x and $-x$. This requirement is satisfied approximately when $k|x|>2.2$. Hence, for relative small wavenumber, we may need more effective families of probing functions that can also separate inhomogeneous inclusions that are close to each other.

3.2. A family of probing functions that improves the accuracy of reconstruction in angular direction

In this subsection, we propose a family of probing functions that can recover the support of inhomogeneous inclusions of different types more accurately compared with the family (3.7)-(3.8). In particular, the resulting kernel functions are sharper in the angular direction, i.e., the direction parallel to the measurement surface, which would enhance the resolution effect. We choose a second order differential operator acting component-wisely on the kernel function $\Im\{\Phi_x(z)\}$.

Considering the symmetry of the sampling domain $B(0,1)$, we first apply the spherical Laplacian $(-\Delta_{\mathbb{S}^2})$ on the kernel function $\Im\{\Phi_x(z)\}$ to improve the sharpness of reconstruction in the angular direction. Using the spherical Laplacian of spherical vector waves (cf. (A.8)) and the expansion of $\Im\{\Phi_x(z)\}$ in (3.3), we have

$$\begin{aligned}|(-\Delta_{\mathbb{S}^2})\Im\{\Phi_x(z)\}| = &-\sum_{m,n}(n^2+n)\Big[\boldsymbol{v}_{1,m,n}(x)\boldsymbol{v}^{\dagger}_{1,m,n}(z)+\boldsymbol{v}_{2,m,n}(x)\boldsymbol{v}^{\dagger}_{2,m,n}(z)\Big]\\ &+\sum_{m,n}2(n^2+n)^{\frac{1}{2}}\boldsymbol{v}_{2,m,n}(x)\boldsymbol{v}^{\dagger}_{3,m,n}(z)\,.\end{aligned} \tag{3.17}$$

However, this kernel function seems to be not so satisfactory from the numerical perspective since the maximum can not be ensured at $x=z$. Intuitively, it is expected that the first part in the representation (3.17) should reach a maximum at $x=z$ due to the symmetry of all the terms associated.

Hence, we choose to keep only the first part in the representation (3.17) as our desired imaging kernel function and verify that it can provide more accurate reconstruction results compared with those in section 3.1. For the notational sake, we define for $\gamma\in\mathbb{N}$ the auxiliary matrix-valued functions:

$$\Xi_1^\gamma(x,z) := \sum_{m,n}(n^2+n)^\gamma \Big[\boldsymbol{v}_{1,m,n}(x)\boldsymbol{v}_{1,m,n}^\dagger(z) + \boldsymbol{v}_{2,m,n}(x)\boldsymbol{v}_{2,m,n}^\dagger(z)\Big], \tag{3.18}$$

$$\Xi_2^\gamma(x,z) := \sum_{m,n}(n^2+n)^\gamma \Big[\boldsymbol{v}_{1,m,n}(x)\boldsymbol{v}_{2,m,n}^\dagger(z) + \boldsymbol{v}_{2,m,n}^\dagger(x)\boldsymbol{v}_{1,m,n}(z)\Big]. \tag{3.19}$$

Then we shall construct a new family $\boldsymbol{w}_z^{i,\gamma}$ of probing functions for $i=1,2$ and $z\in\Omega$ such that

$$\langle \nu\times(\Phi_x\cdot\boldsymbol{c}_x),\ \boldsymbol{w}_z^{1,\gamma}\cdot\boldsymbol{p}_z\rangle_{L^2(\partial\Omega)} = \boldsymbol{c}_x^T\,\Xi_1^\gamma(x,z)\boldsymbol{p}_z\,,\quad \langle \nu\times(\Phi_x\cdot\boldsymbol{c}_x),\ \boldsymbol{w}_z^{2,\gamma}\cdot\boldsymbol{q}_z\rangle_{L^2(\partial\Omega)} = \boldsymbol{c}_x^T\,\Xi_2^\gamma(x,z)\boldsymbol{q}_z\,.$$

Using (3.4), we derive

$$\boldsymbol{w}_z^{1,\gamma}(y) := \sum_{m,\,n}(n^2+n)^\gamma\Big[\boldsymbol{v}_{2,m,n}(z)(\boldsymbol{u}_{1,m,n}^\dagger(y)+c_{4,n}\boldsymbol{u}_{4,m,n}^\dagger(y)) + \boldsymbol{v}_{1,m,n}(z)(\boldsymbol{u}_{2,m,n}^\dagger(y)+c_{3,n}\boldsymbol{u}_{3,m,n}^\dagger(y))\Big], \tag{3.20}$$

$$\boldsymbol{w}_z^{2,\gamma}(y) := \sum_{m,\,n}\frac{(n^2+n)^\gamma}{k}\Big[\boldsymbol{v}_{1,m,n}(z)(\boldsymbol{u}_{1,m,n}^\dagger(y)+c_{4,n}\boldsymbol{u}_{4,m,n}^\dagger(y)) + \boldsymbol{v}_{2,m,n}(z)(\boldsymbol{u}_{2,m,n}^\dagger(y)+c_{3,n}\boldsymbol{u}_{3,m,n}^\dagger(y))\Big], \tag{3.21}$$

and the corresponding index functions for reconstructing Ω_ϵ and Ω_μ:

$$I_{mo}^\gamma(z) := \frac{\langle \nu\times E^s,\ \boldsymbol{w}_z^{1,\gamma}\cdot\boldsymbol{p}_z\rangle_{L^2(\partial\Omega)}}{n^\gamma(z)}\,,\quad I_{di}^\gamma(z) := \frac{\langle \nu\times E^s,\ \boldsymbol{w}_z^{2,\gamma}\cdot\boldsymbol{q}_z\rangle_{L^2(\partial\Omega)}}{n^\gamma(z)}\,, \tag{3.22}$$

where $n^\gamma(z) := |\sum \mathrm{diag}\{\Xi_1^\gamma(z,z)\}|^{\frac{1}{2}}$, whose choice will be explained in section 3.2.2.

3.2.1. Verification of the mutually almost orthogonality property in angular direction

We now verify the previous probing functions $\boldsymbol{w}_z^{1,\gamma}(y)$ and $\boldsymbol{w}_z^{2,\gamma}(y)$ have the desired mutually almost orthogonality property through a careful investigation of the kernel functions as defined in (2.15):

$$K^{1,\gamma}_{\boldsymbol{c}_x,\boldsymbol{p}_z}(x,z) = K^{4,\gamma}_{\boldsymbol{c}_x,\boldsymbol{p}_z}(x,z) = \frac{\boldsymbol{c}_x\Xi_1^\gamma(x,z)\boldsymbol{p}_z}{n^\gamma(z)}\,,\quad \frac{1}{k}K^{2,\gamma}_{\boldsymbol{d}_x,\boldsymbol{p}_z}(x,z) = kK^{3,\gamma}_{\boldsymbol{d}_x,\boldsymbol{p}_z}(x,z) = \frac{\boldsymbol{d}_x\Xi_2^\gamma(x,z)\boldsymbol{p}_z}{n^\gamma(z)}\,. \tag{3.23}$$

Especially, we show that $K^{1,\gamma}_{\boldsymbol{c}_x,\boldsymbol{p}_z}(x,z)$ reaches a maximum at $\hat{z}=\hat{x}$ and becomes sharper, i.e. decaying faster, as γ becomes larger in the angular direction in section 3.2.1, and it reaches a maximum when $r_z=r_x$ in section 3.2.2. The decoupling effect, i.e. the magnitude of $K^{2,\gamma}_{\boldsymbol{d}_x,\boldsymbol{p}_z}(x,z)$ is small under any circumstances, is verified through theoretical justifications in this subsection and numerical experiments in section 3.2.2.

To check if $K^{1,\gamma}_{\boldsymbol{c}_x,\boldsymbol{p}_z}(x,z)$ becomes sharper in angular direction as γ grows, we notice that the expansion (3.18) can be formulated by summing up the first and second kind of spherical vector waves along with the m indices first and then summing up along with the n indices under the weight $(n^2+n)^\gamma$. Hence, we may define

$$\begin{aligned} L_n(x,z) := \sum_m \Big[& f_1^n(kr_x)f_1^n(kr_z)A_{1,m,n}(\hat{x})A_{1,m,n}^\dagger(\hat{z}) \\ & + (f_2^n(kr_x)A_{2,m,n}(\hat{x}) + (n^2+n)^{\frac{1}{2}}f_3^n(kr_x)A_{3,m,n}(\hat{x}))(f_2^n(kr_z)A_{2,m,n}^\dagger(\hat{z}) + (n^2+n)^{\frac{1}{2}}f_3^n(kr_z)A_{3,m,n}^\dagger(\hat{z}))\Big], \end{aligned} \tag{3.24}$$

where $\sum_m$ represents the summation over $-n\le m\le n$ and

$$f_1^n(kr) := j_n(kr)\,,\quad f_2^n(kr) := \frac{(krj_n(kr))'}{kr}\,,\quad f_3^n(kr) := \frac{j_n(kr)}{kr}\,, \tag{3.25}$$

with $j_n(kr)$ being the spherical Bessel function of first kind of order n.

For simplicity, we write $f_{i,x}^n = f_i^n(kr_x)$, $f_{i,z}^n = f_i^n(kr_z)$ for $i=1,2,3$ below. We first see $\Xi_1^\gamma(x,z) = \sum_n (n^2+n)^\gamma L_n(x,z)$. We notice that if $\boldsymbol{d}^T L_n(x,z)\boldsymbol{d}$ achieves the maximum at $z=x$ with $\boldsymbol{d}^T L_n(x,x)\boldsymbol{d}\ge 0$ for each n and some direction $\boldsymbol{d}$, then $\boldsymbol{d}^T\Xi_1^\gamma(x,z)\boldsymbol{d} = \sum_n(n^2+n)^\gamma\boldsymbol{d}^T L_n(x,z)\boldsymbol{d}$ also achieves the maximum at $z=x$. Moreover, if $L_n(x,z)$ becomes sharper as n grows, then Ξ_1^γ will be also sharper since $(n_2^2+n_2)^\gamma/(n_1^2+n_1)^\gamma$ increases with γ for any $n_2>n_1$.

With the above observation, we next work out a closed form of $L_n(x,z)$ and then study its properties. We first recall an identity and a transformation matrix from Cartesian to spherical coordinates:

$$\frac{4\pi}{2n+1}\sum_m Y_n^m(\hat{x})\overline{Y_n^m}(\hat{z}) = P_n(\hat{x}\cdot\hat{z})\,,\quad \gamma(\hat{x}) = \begin{pmatrix} \sin\theta_x\cos\phi_x & \sin\theta_x\sin\phi_x & \cos\theta_x \\ \cos\theta_x\cos\phi_x & \cos\theta_x\sin\phi_x & -\sin\theta_x \\ -\sin\phi_x & \cos\phi_x & 0 \end{pmatrix}.$$

Assuming $\boldsymbol{c}_x=\boldsymbol{p}_z=\boldsymbol{d}$, and denoting $\boldsymbol{d}_x = \gamma(\hat{x})\boldsymbol{d} = d_r^x\hat{\boldsymbol{r}}_x + d_\theta^x\hat{\boldsymbol{\theta}}_x + d_\phi^x\hat{\boldsymbol{\phi}}_x$, we have $\boldsymbol{d}_z = \gamma(\hat{z})\gamma^T(\hat{x})\boldsymbol{d}_x$.

Now, writing $t = \hat{x}\cdot\hat{z}$, denoting P_n^m as the associated Legendre polynomial, and using the products of vector spherical harmonics in (A.4), we derive

$$\begin{aligned}
&\frac{4\pi}{2n+1}\boldsymbol{d}^T L_n(x,z)\boldsymbol{d} = f_{3,x}^n f_{3,z}^n d_r^x d_r^z P_n(t) \\
&+\frac{f_{2,x}^n f_{2,z}^n}{n^2+n}\Big[\frac{d_\phi^x d_\phi^z}{\sin\theta_x\sin\theta_z}\Big\{\frac{\partial^2 t}{\partial\phi_x\partial\phi_z}\frac{-P_n^1(t)}{\sqrt{1-t^2}}+\frac{\partial t}{\partial\phi_x}\frac{\partial t}{\partial\phi_z}\frac{P_n^2(t)}{1-t^2}\Big\}+d_\theta^x d_\theta^z\Big\{\frac{\partial^2 t}{\partial\theta_x\partial\theta_z}\frac{-P_n^1(t)}{\sqrt{1-t^2}}+\frac{\partial t}{\partial\theta_x}\frac{\partial t}{\partial\theta_z}\frac{P_n^2(t)}{1-t^2}\Big\} \\
&\qquad+\Big\{\frac{d_\theta^x d_\phi^z}{\sin\theta_z}\frac{\partial t}{\partial\phi_z}\frac{\partial t}{\partial\theta_x}+\frac{d_\phi^x d_\theta^z}{\sin\theta_x}\frac{\partial t}{\partial\phi_x}\frac{\partial t}{\partial\theta_z}\Big\}\frac{P_n^2(t)}{1-t^2}+\Big\{\frac{d_\theta^x d_\phi^z}{\sin\theta_z}\frac{\partial^2 t}{\partial\phi_z\partial\theta_x}+\frac{d_\phi^x d_\theta^z}{\sin\theta_x}\frac{\partial^2 t}{\partial\phi_x\partial\theta_z}\Big\}\frac{(-P_n^1(t))}{\sqrt{1-t^2}}\Big] \\
&+\frac{f_{1,x}^n f_{1,z}^n}{n^2+n}\Big[\frac{d_\theta^x d_\theta^z}{\sin\theta_x\sin\theta_z}\Big\{\frac{\partial^2 t}{\partial\phi_x\partial\phi_z}\frac{-P_n^1(t)}{\sqrt{1-t^2}}+\frac{\partial t}{\partial\phi_x}\frac{\partial t}{\partial\phi_z}\frac{P_n^2(t)}{1-t^2}\Big\}+d_\phi^x d_\phi^z\Big\{\frac{\partial^2 t}{\partial\theta_x\partial\theta_z}\frac{-P_n^1(t)}{\sqrt{1-t^2}}+\frac{\partial t}{\partial\theta_x}\frac{\partial t}{\partial\theta_z}\frac{P_n^2(t)}{1-t^2}\Big\} \\
&\qquad-\Big\{\frac{d_\phi^x d_\theta^z}{\sin\theta_z}\frac{\partial t}{\partial\phi_z}\frac{\partial t}{\partial\theta_x}+\frac{d_\theta^x d_\phi^z}{\sin\theta_x}\frac{\partial t}{\partial\phi_x}\frac{\partial t}{\partial\theta_z}\Big\}\frac{P_n^2(t)}{1-t^2}-\Big\{\frac{d_\phi^x d_\theta^z}{\sin\theta_z}\frac{\partial^2 t}{\partial\phi_z\partial\theta_x}+\frac{d_\theta^x d_\phi^z}{\sin\theta_x}\frac{\partial^2 t}{\partial\phi_x\partial\theta_z}\Big\}\frac{(-P_n^1(t))}{\sqrt{1-t^2}}\Big] \\
&+\frac{f_{3,x}^n f_{2,z}^n}{\sqrt{n^2+n}}\Big[d_r^x d_\theta^z\frac{\partial t}{\partial\theta_x}+\frac{d_r^x d_\phi^z}{\sin\theta_x}\frac{\partial t}{\partial\phi_x}\Big]\frac{(-P_n^1(t))}{\sqrt{1-t^2}}+\frac{f_{2,x}^n f_{3,z}^n}{\sqrt{n^2+n}}\Big[d_\theta^x d_r^z\frac{\partial t}{\partial\theta_z}+\frac{d_\phi^x d_r^z}{\sin\theta_z}\frac{\partial t}{\partial\phi_z}\Big]\frac{(-P_n^1(t))}{\sqrt{1-t^2}}\,.
\end{aligned}\tag{3.26}$$

With the closed form above, we now study its behavior in the angular direction by assuming $r_z = r_x = r_0$. Moreover, considering the symmetry of domain $B(0,1)$, without loss of generality, we further assume $\phi_z = \phi_x$ and investigate the behavior of $\boldsymbol{d}^T L_n(x,z)\boldsymbol{d}$ for fixed x, $\boldsymbol{d}$, and $\theta_z \in [0,\pi]$. In particular, we will show that the normalization term $n^\gamma(z)$ in (3.22) depends only on r_z (see (3.44)), so we write $n^\gamma(r_0) = n^\gamma(z)$ below.

Using the identity $\boldsymbol{d}_z = \gamma(\hat{z})\gamma^T(\hat{x})\boldsymbol{d}_x$ to convert the dependence of direction with respect to z to x, i.e.,

$$d_r^z = \cos(\theta_x-\theta_z)d_r^x - \sin(\theta_x-\theta_z)d_\theta^x\,,\ d_\theta^z = \sin(\theta_x-\theta_z)d_r^x + \cos(\theta_x-\theta_z)d_\theta^x\,,\ d_\phi^z = d_\phi^x\,,\ \text{when } \phi_x=\phi_z\,,$$

we can simplify (3.26) as

$$\begin{aligned}
\frac{4\pi}{2n+1}\boldsymbol{d}^T L_n(x,z)\boldsymbol{d} =& \frac{|j_n(kr_0)|^2}{k^2r_0^2(n^2+n)}|d_\phi^x|^2\Big[(n^2+n)P_n(t)+\frac{tP_n^1(t)}{\sqrt{1-t^2}}\Big]+\frac{|(kr_0j_n(kr_0))'|^2}{k^2r_0^2(n^2+n)}|d_\phi^x|^2\frac{-P_n^1(t)}{\sqrt{1-t^2}} \\
&+t\Big\{\frac{|j_n(kr_0)|^2}{k^2r_0^2}P_n(t)+|d_\theta^x|^2\frac{|(kr_0j_n(kr_0))'|^2}{k^2r_0^2(n^2+n)}\Big[(n^2+n)P_n(t)+\frac{tP_n^1(t)}{\sqrt{1-t^2}}\Big] \\
&+\frac{|j_n(kr_0)|^2}{k^2r_0^2(n^2+n)}|d_\theta^x|^2\frac{-P_n^1(t)}{\sqrt{1-t^2}}\Big\}+\sqrt{1-t^2}g(t)\,,
\end{aligned}\tag{3.27}$$

where

$$\begin{aligned}
g(t) =& d_\theta^x\Big\{\frac{|(kr_0j_n(kr_0))'|^2}{k^2r_0^2(n^2+n)}\Big[(n^2+n)P_n(t)+\frac{tP_n^1(t)}{\sqrt{1-t^2}}\Big]-\frac{|j_n(kr_0)|^2}{n^2+n}\frac{P_n^1(t)}{\sqrt{1-t^2}} \\
&+\frac{|j_n(kr_0)|^2}{k^2r_0^2}P_n(t)+2\sqrt{1-t^2}\frac{(kr_0j_n(kr_0))'j_n(kr_0)}{k^2r_0^2\sqrt{n^2+n}}\frac{P_n^1(t)}{\sqrt{1-t^2}}\Big\}\,.
\end{aligned}$$

Noting that $g(t)$ is bounded for all t and $\sqrt{1-t^2}$ vanishes at $t=1$ (i.e., $\hat{x}=\hat{z}$), we may treat $\sqrt{1-t^2}g(t)$ as a small term when $\hat{z}$ is close to $\hat{x}$. We now recall properties of Legendre polynomials and can show that

$$P_n(t)\,,\quad (n^2+n)P_n(t)+\frac{tP_n^1(t)}{\sqrt{1-t^2}}\,,\quad \text{and}\quad -\frac{P_n^1(t)}{\sqrt{1-t^2}}$$

as well as these terms multiplied by t all achieve a positive maximum at $t=1$ for $t\in[-1,1]$ (i.e., $\hat{z}=\hat{x}$), by using their generating functions. Therefore, using the fact that the coefficients associated with those Legendre polynomials are all positive in (3.27), $\boldsymbol{d}^T L_n(x,z)\boldsymbol{d}$ achieves its maximum at $\hat{z}\approx\hat{x}$ when $r_z = r_x$.

Furthermore, by the recursive relations of Legendre polynomials, we can compute their derivatives at $t=1$:

$$\begin{aligned}
&\frac{d}{dt}tP_n(t)\Big|_{t=1} = \frac{n^2+n+2}{2}\,,\quad \frac{d}{dt}\frac{-P_n^1(t)}{\sqrt{1-t^2}}\Big|_{t=1} = \frac{(n^3-n)(n+2)}{8}\,,\quad \frac{d}{dt}\frac{-tP_n^1(t)}{\sqrt{1-t^2}}\Big|_{t=1} = \frac{n(n+1)(n^2+2n+2)}{8}\,, \\
&\frac{d}{dt}\Big((n^2+n)P_n(t)+\frac{tP_n^1(t)}{\sqrt{1-t^2}}\Big)\Big|_{t=1} = \frac{(n^2+n)(3n^2+3n-2)}{8}\,, \\
&\frac{d}{dt}t\Big[\Big((n^2+n)P_n(t)+\frac{P_n^1(t)}{\sqrt{1-t^2}}\Big)\Big]\Big|_{t=1} = \frac{(n^2+n)(3n^2+3n+2)}{8}\,.
\end{aligned}\tag{3.28}$$

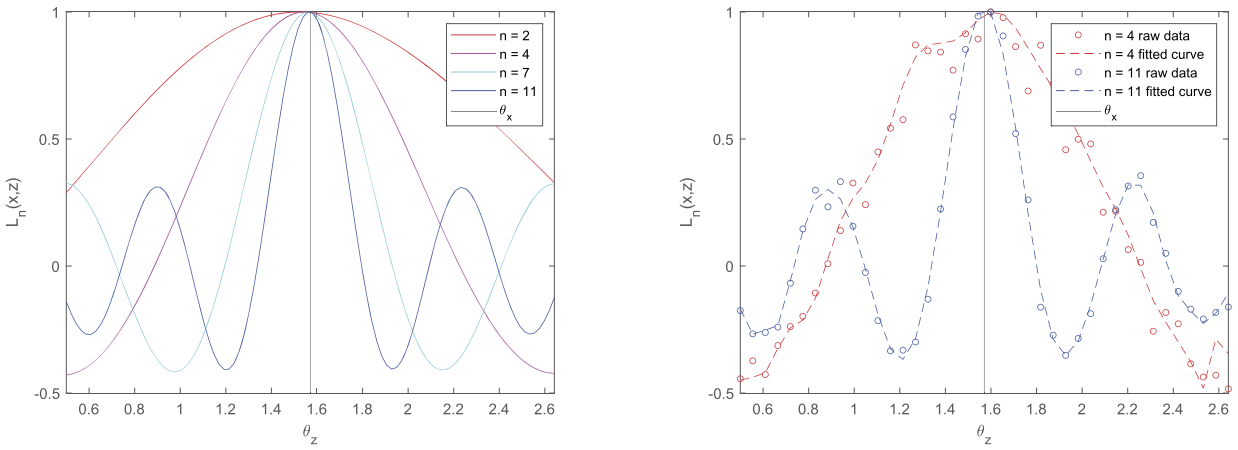

Fig. 1. Values of $\boldsymbol{c}_x^T L_n(x,z)\boldsymbol{p}_z$ for $r_z = r_x = 0.5$, $\phi_x = \phi_x = \frac{\pi}{2}$, $\theta_x = \frac{\pi}{2}$, and $\theta_z \in [0.5, \pi - 0.5]$ with different n. Left plot: $\boldsymbol{c}_x = \boldsymbol{p}_z = (1,1,1)^T/\sqrt{3}$ for $n = 2, 4, 7, 11$; Right plot: $\boldsymbol{c}_x = (1,1,1)^T/\sqrt{3}$, $\boldsymbol{p}_z = \boldsymbol{c}_x + 0.1(\epsilon_1, \epsilon_2, \epsilon_3)^T$, with $\epsilon_i \sim \mathcal{N}(0,1)$ for $i = 1, 2, 3$; $n = 4, 11$.

We see that as n grows, all the above functions decay faster when t decreases from 1, hence the magnitude of $\boldsymbol{d}^T L_n(x,z)\boldsymbol{d}$ decays also faster for z along any direction that points away from x when $r_z = r_x$.

In Fig. 1, we plot $\boldsymbol{c}_x^T L_n(x,z)\boldsymbol{p}_z$ for $n = 2, 4, 7, 11$ and $r_z = r_x = 0.5$, $\phi_z = \phi_x = \frac{\pi}{2}$, $\theta_x = \frac{\pi}{2}$, and $\theta_z \in [0.5, \pi - 0.5]$. In the plots on the left and right, we assume $\boldsymbol{c}_x = \boldsymbol{p}_z = (1,1,1)^T/\sqrt{3}$ for all z, and $\boldsymbol{c}_x = (1,1,1)^T/\sqrt{3}$ and $\boldsymbol{p}_z = \boldsymbol{c}_x + 0.1(\epsilon_1, \epsilon_2, \epsilon_3)^T$, respectively, with $\epsilon_i \sim \mathcal{N}(0,1)$ for $i = 1, 2, 3$. The left plot validates our previous prediction on the property of $\boldsymbol{d}^T L_n(x,z)\boldsymbol{d}$ that it achieves the maximum at $z \approx x$ for all n, and as n becomes larger the function decays faster when z goes away from x. The right plot considers the case that $\boldsymbol{p}_z$ is only a very rough approximation to $\boldsymbol{c}_x$, i.e., $\boldsymbol{p}_z = \boldsymbol{c}_x + +0.1(\epsilon_1, \epsilon_2, \epsilon_3)^T$, with $\epsilon_i \sim \mathcal{N}(0,1)$ for $i = 1, 2, 3$ which is the usual situation in practice. We notice that the orthogonality property still holds as the value of $\boldsymbol{d}^T L_n(x,z)\boldsymbol{d}$ achieve the maximum at $z \approx x$ and decays faster as n becomes larger.

Therefore, based on our discussions at the beginning part of this subsection about the relation between $L_n(x,z)$ and $K^{1,\gamma}_{\boldsymbol{c}_x,\boldsymbol{p}_z}(x,z)$ under $\boldsymbol{p}_z \approx \boldsymbol{c}_x$, the kernel function $K^{1,\gamma}_{\boldsymbol{c}_x,\boldsymbol{p}_z}(x,z) = \sum_n (n^2+n)^\gamma \boldsymbol{c}_x^T L_n(x,z)\boldsymbol{p}_z / n^\gamma(r_0)$ will achieve a maximum at $z \approx x$ when $r_z = r_x = r_0$. Moreover, as γ increases, $K^{1,\gamma}_{\boldsymbol{c}_x,\boldsymbol{p}_z}(x,z)$ decays faster when z moves away from x.

We can extend the above discussions for $\Xi_1^\gamma(x,z)$ to $\Xi_2^\gamma(x,z)$ (cf. (3.18)) to validate that $K^{2,\gamma}_{\boldsymbol{d}_x,\boldsymbol{p}_z}(x,z)$ does not achieve a local maximum at $z = x$. Similarly to the definition of L_n in (3.24), we introduce

$$\begin{aligned}\widetilde{L}_n(x,z) := \sum_m \Big[& f^n_{1,x} A_{1,m,n}(\hat{x}) (f^n_{2,z} A^\dagger_{2,m,n}(\hat{z}) + (n^2+n)^{\frac{1}{2}} f^n_{3,z} (A^\dagger_{3,m,n}(\hat{z})) \\ & + (f^n_{2,x} A_{2,m,n}(\hat{x}) + (n^2+n)^{\frac{1}{2}} f^n_{3,x} A_{3,m,n}(\hat{x})) f^n_{1,z} A^\dagger_{1,m,n}(\hat{z}) \Big],\end{aligned} \tag{3.29}$$

then we have $\Xi_2^\gamma(x,z) = \sum_n (n^2+n)^\gamma \widetilde{L}_n(x,z)$, where $f_{i,x}$, $f_{i,z}$ are defined as in (3.24).

To work out a closed form of $\widetilde{L}_n$, we use the products of vector spherical harmonics (cf. (A.4)) to obtain for arbitrary directions $\boldsymbol{d}_x$ and $\boldsymbol{p}_z$,

$$\begin{aligned}&\frac{4\pi}{2n+1}\boldsymbol{d}_x^T \widetilde{L}_n(x,z)\boldsymbol{p}_z \\ =& d^x_r p^z_\theta f^n_{3,x} f^n_{1,z} \frac{dP_n(t)}{\sin\theta_x d\phi_x} + d^x_\theta p^z_r f^n_{3,z} f^n_{1,x} \frac{dP_n(t)}{\sin\theta_z d\phi_z} - d^x_r p^z_\phi f^n_{3,x} f^n_{1,z} \frac{dP_n(t)}{d\theta_z} - d^x_\phi p^z_r f^n_{3,z} f^n_{1,x} \frac{dP_n(t)}{d\theta_x} \\ &+ \frac{d^x_\theta p^z_\theta}{n^2+n}\Big[f^n_{1,x} f^n_{2,z} \frac{d^2P_n(t)}{\sin\theta_x d\phi_x d\theta_z} + f^n_{2,x} f^n_{1,z} \frac{d^2P_n(t)}{\sin\theta_z d\theta_x d\phi_z} \Big] - \frac{d^x_\phi p^z_\phi}{n^2+n}\Big[f^n_{1,x} f^n_{2,z} \frac{d^2P_n(t)}{\sin\theta_z d\theta_x d\phi_z} + f^n_{2,x} f^n_{1,z} \frac{d^2P_n(t)}{\sin\theta_x d\phi_x d\theta_z} \Big] \\ &+ \frac{d^x_\theta p^z_\phi}{n^2+n}\Big[f^n_{1,x} f^n_{2,z} \frac{d^2P_n(t)}{\sin\theta_x \sin\theta_z d\phi_x d\phi_z} - f^n_{2,x} f^n_{2,z} \frac{d^2P_n(t)}{d\theta_x d\theta_z} \Big] \\ &- \frac{d^x_\phi d^z_\theta}{n^2+n}\Big[f^n_{1,x} f^n_{2,z} \frac{d^2P_n(t)}{d\theta_x \theta_z} - f^n_{2,x} f^n_{2,z} \frac{d^2P_n(t)}{\sin\theta_x \sin\theta_z d\phi_x d\phi_z} \Big].\end{aligned} \tag{3.30}$$

This can be simplified under the condition that $\phi_z = \phi_x$:

$$\frac{4\pi}{2n+1}\boldsymbol{d}_x^T \widetilde{L}_n(x,z)\boldsymbol{p}_z = \sqrt{1-t^2}\tilde{g}(t) - \Big(\frac{f^n_{2,x} f^n_{2,z}}{n^2+n} d^x_\theta p^z_\phi + \frac{f^n_{1,x} f^n_{2,z}}{n^2+n} d^x_\phi p^z_\theta \Big) \Big[(n^2+n) P_n(t) + \frac{t P^1_n(t)}{\sqrt{1-t^2}} \Big]$$

$$-\Big(\frac{f^n_{2,x}f^n_{2,z}}{n^2+n}d^x_\phi p^z_\theta+\frac{f^n_{1,x}f^n_{2,z}}{n^2+n}d^x_\theta p^z_\phi\Big)\frac{P^1_n(t)}{\sqrt{1-t^2}}\,, \tag{3.31}$$

where $\tilde{g}(t)=-(d^x_r p^z_\phi f^n_{3,x}f^n_{1,z}-d^x_\phi p^z_r f^n_{3,z}f^n_{1,x})\frac{P^1_n(t)}{\sqrt{1-t^2}}$ is bounded for all t. At $z=x$, we can see from (3.31) that

$$\frac{4\pi}{2n+1}\boldsymbol{d}_x^T\widetilde{L}_n(x,x)\boldsymbol{p}_z=\sqrt{1-(\boldsymbol{c}_x\cdot\boldsymbol{p}_z)^2}\frac{(kr_z j_n(kr_x))'}{2kr_x}\Big[(1+\frac{n}{kr_x})j_n(kr_x)-j_{n-1}(kr_x)\Big].$$

Hence the above term and also $K^{2,\gamma}_{\boldsymbol{d}_x,\boldsymbol{p}_z}(x,x)=\sum_n \boldsymbol{d}_x^T\widetilde{L}_n(x,x)\boldsymbol{p}_z/n^\gamma(r_0)$ are approximately 0 when $\boldsymbol{p}_z\approx\boldsymbol{d}_x$. This implies that $I_{mo}(x)$ has no local maximum at the point x associated with a magnetic monopole. In fact, by our earlier discussions about $K^{1,\gamma}_{\boldsymbol{c}_x,\boldsymbol{p}_z}(x,z)$, a local maximum will appear for $I_{di}(x)$. As we see from Fig. 2 in the next subsection, numerical experiments for more general cases are conducted to verify that the magnitude of $K^{2,\gamma}_{\boldsymbol{d}_x,\boldsymbol{p}_z}(x,z)$ is much smaller compared with $K^{1,\gamma}_{\boldsymbol{c}_x,\boldsymbol{p}_z}(x,z)$ in the whole sampling domain.

3.2.2. Verification of the mutually almost orthogonality property in the radial direction and the whole sampling domain

In the previous section 3.2.1, we have shown that the family of probing functions (3.20)-(3.21) has the desired mutually almost orthogonality property in the angular direction. In particular, the sharpness of the corresponding kernel function can be clearly improved as γ increases. In this subsection, to verify the mutually almost orthogonality property in the radial direction, we first present a closed form of the kernel function $K^{1,1}_{\boldsymbol{c}_x,\boldsymbol{p}_z}$ in (2.15) for us to have a better understanding of the normalization term $n^\gamma(z)$ we chose in (3.22). To simplify our upcoming discussion, we will focus on the case $\gamma=1$, which is a preferable choice in practice. More illustrations about the parameter choice can be found at the end of this subsection.

Firstly, with a similar argument as in proving Lemma 3.1, we can derive

$$\frac{\sin(k|x-z|)}{|x-z|}\boldsymbol{I}_3=ik\sum_{m,n}\Big[\boldsymbol{v}_{1,m,n}(x)\boldsymbol{v}^\dagger_{1,m,n}(z)+\boldsymbol{v}_{2,m,n}(x)\boldsymbol{v}^\dagger_{2,m,n}(z)+\boldsymbol{v}_{3,m,n}(x)\boldsymbol{v}^\dagger_{3,m,n}(z)\Big]. \tag{3.32}$$

For the notational sake, we write

$$F(x,z):=r_x^2(-\Delta_{\mathbb{S}^2(x)})\frac{\sin(k|x-z|)}{|x-z|}\,, \tag{3.33}$$

then by means of the spherical Laplacian of spherical vector waves (cf. (A.8)), we obtain

$$\begin{aligned}F(x,z)\boldsymbol{I}_3=&-\sum_{\substack{\tau=1,2,3\\m,n}}(n^2+n)\boldsymbol{v}_{\tau,m,n}(x)\boldsymbol{v}^\dagger_{\tau,m,n}(z)\\&-\sum_{m,n}2\Big[\boldsymbol{v}_{3,m,n}(x)\boldsymbol{v}^\dagger_{3,m,n}(z)-2\sqrt{n^2+n}\Big(\boldsymbol{v}_{3,m,n}(x)\boldsymbol{v}^\dagger_{2,m,n}(z)+\boldsymbol{v}_{2,m,n}(x)\boldsymbol{v}^\dagger_{3,m,n}(z)\Big)\Big].\end{aligned} \tag{3.34}$$

Comparing (3.34) and the definition of $\Xi^1_1(x,z)$ in (3.18), we can get $\Xi^1_1(x,z)$ by removing the terms in $F(x,z)$ that are associated with $\boldsymbol{v}_{3,m,n}$. Indeed, we obtain by noting $\nabla_x\times\boldsymbol{v}_{3,m,n}(x)=0$ and $\nabla\times\nabla\times\boldsymbol{v}_{i,m,n}=k^2\boldsymbol{v}_{i,m,n}$ for $i=1,2$,

$$k^2\Xi^1_1(x,z)=\nabla_x\times\nabla_z\times(F(x,z)\boldsymbol{I}_3)=\begin{bmatrix}\frac{\partial^2F}{\partial z_3\partial x_3}+\frac{\partial^2F}{\partial z_2\partial x_2} & -\frac{\partial^2F}{\partial z_1\partial x_2} & -\frac{\partial^2F}{\partial z_1\partial x_3}\\ -\frac{\partial^2F}{\partial z_2\partial x_1} & \frac{\partial^2F}{\partial z_1\partial x_1}+\frac{\partial^2F}{\partial z_3\partial x_3} & -\frac{\partial^2F}{\partial z_2\partial x_3}\\ -\frac{\partial^2F}{\partial z_3\partial x_1} & -\frac{\partial^2F}{\partial z_3\partial x_2} & \frac{\partial^2F}{\partial z_1\partial x_1}+\frac{\partial^2F}{\partial z_2\partial x_2}\end{bmatrix}. \tag{3.35}$$

Hence, it is possible to compute explicit representations of kernel functions defined in (2.15) by using $F(x,z)$ due to the relationship between Ξ^1_1 and the kernel function in (3.23). Firstly, we present a closed form of $F(x,z)$ by its definition in (3.33):

$$F(x,z)=r_x^2k^2s_0(x-z)+\Big(\frac{2(r_x^2-x\cdot z)}{|x-z|}+\frac{r_x^2}{|x-z|}-\frac{(r_x^2-x\cdot z)^2}{|x-z|^3}\Big)s_1(x-z)+\frac{(r_x^2-x\cdot z)^2}{|x-z|^2}s_2(x-z)\,,$$

where $s_j(x-z):=\frac{\partial^j}{\partial|x-z|^j}\frac{\sin(k|x-z|)}{|x-z|}$. Then we can compute the partial derivative of $F(x,z)$ $(i,j=1,2,3)$:

$$\frac{\partial^2}{\partial x_i\partial z_j}F(x,z)=s_1(x-z)\underbrace{\Big[\frac{\partial^2t_1(x,z)}{\partial x_i\partial z_j}+\Big(\frac{\partial^2|x-z|}{\partial x_i\partial z_j}+\frac{\partial|x-z|}{\partial x_i}\frac{\partial}{\partial z_j}+\frac{\partial|x-z|}{\partial z_j}\frac{\partial}{\partial x_i}\Big)t_0(x,z)\Big]}_{c_1(x,z)} \tag{3.36}$$

$$+ s_2(x-z)\underbrace{\Big[\frac{\partial^2 t_2(x,z)}{\partial x_i \partial z_j} + \Big(\frac{\partial |x-z|^2}{\partial x_i \partial z_j} + \frac{\partial |x-z|}{\partial x_i}\frac{\partial}{\partial z_j} + \frac{\partial |x-z|}{\partial z_j}\frac{\partial}{\partial x_i}\Big) t_1(x,z) - \frac{d_i d_j}{|x-z|^2} t_0(x,z)\Big]}_{c_2(x,z)}$$

$$+ s_3(x-z)\underbrace{\Big[\Big(\frac{\partial^2 |x-z|}{\partial x_i \partial z_j} + \frac{\partial |x-z|}{\partial x_i}\frac{\partial}{\partial z_j} + \frac{\partial |x-z|}{\partial z_j}\frac{\partial}{\partial x_i}\Big) t_2(x,z) - \frac{d_i d_j}{|x-z|^2} t_1(x,z)\Big]}_{c_3(x,z)} - s_4(x-z)\underbrace{\Big[\frac{d_i d_j}{|x-z|^2} t_2(x,z)\Big]}_{c_4(x,z)},$$

where $d_i = (x-z)_i$ and

$$t_0(x,z) = r_x^2 k^2\,, \quad t_1(x,z) = \frac{2(r_x^2 - x\cdot z)}{|x-z|} + \frac{r_x^2}{|x-z|} - \frac{(r_x^2 - x\cdot z)^2}{|x-z|^3}\,, \quad t_2(x,z) = \frac{(r_x^2 - x\cdot z)^2}{|x-z|^2}\,.$$

Denoting $c_i(x,z)$ as the coefficient associated with s_i in (3.36), that is $\frac{\partial^2 F(x,z)}{\partial x_i \partial z_j} = \sum_{i=1,2,3,4} s_i(x-z) c_i(x,z)$. Then $c_4(x,z)$ can first be simplified as

$$c_4(x,z) = -\frac{d_i d_j}{|x-z|^4}(r_x^2 - x\cdot z)^2\,. \tag{3.37}$$

Noting that $\frac{\partial^2 |x-z|}{\partial x_i \partial z_j} = -\delta_{i,j}/|x-z| + d_i d_j/|x-z|^3$, then $c_3(x,z)$ becomes

$$\begin{aligned} c_3(x,z) =& -\delta_{i,j}\frac{(r_x^2 - x\cdot z)^2}{|x-z|^3} + d_i d_j\Big(-\frac{r_x^2}{|x-z|^3} - 4\frac{(r_x^2 - x\cdot z)}{|x-z|^3} + 6\frac{(r_x^2 - x\cdot z)^2}{|x-z|^5}\Big) \\ & - 2\frac{(r_x^2 - x\cdot z)(d_i x_j + x_i d_j)}{|x-z|^3}\,. \end{aligned} \tag{3.38}$$

For $c_2(x,z)$ and $c_1(x,z)$, we first keep the term $\frac{\partial^2}{\partial x_i \partial z_j} t_1(x,z)$ as a whole, then

$$c_2(x,z) = -2\delta_{i,j} - k^2 r_x^2 \frac{d_i d_j}{|x-z|^2} - |x-z|\frac{\partial^2}{\partial x_i \partial z_j} t_1(x,z)\,, \tag{3.39}$$

$$c_1(x,z) = \frac{\partial^2}{\partial x_i \partial z_j} t_1(x,z) + \Big(-\frac{\delta_{i,j}}{|x-z|} + \frac{d_i d_j}{|x-z|^3}\Big) k^2 r_x^2 - \frac{2k^2 d_j x_i}{|x-z|}\,. \tag{3.40}$$

For the term $\frac{\partial^2}{\partial x_i \partial z_j} t_1(x,z)$, we have

$$\begin{aligned} \frac{\partial^2}{\partial x_i \partial z_j} t_1(x,z) =& \delta_{i,j}\Big(\frac{-2}{|x-z|} + \frac{r_x^2 + 4(r_x^2 - x\cdot z)}{|x-z|^3} - \frac{3(r_x^2 - x\cdot z)^2}{|x-z|^5}\Big) + 2\frac{2d_i x_j + 2x_i d_j + d_i d_j + x_i x_j}{|x-z|^3} \\ & - \frac{3d_i d_j r_x^2}{|x-z|^5} - 6\frac{(r_x^2 - x\cdot z)(2d_i d_j + d_i x_j + x_i d_j)}{|x-z|^5} + 15 d_i d_j \frac{(r_x^2 - x\cdot z)^2}{|x-z|^7}\,. \end{aligned} \tag{3.41}$$

Recall that we are mainly interested in the behavior of kernel functions in the radial direction in this subsection, so we assume $\hat{x} = \hat{z}$ that leads to $x\cdot z = r_x r_z$ and $r_x^2 - x\cdot z = r_x(r_x - r_z)$. Denoting $\beta_i = x_i/r_x = z_i/r_z$, then from (3.37) to (3.40), $c_i(x,z)$ for $i = 1,2,3,4$ can be simplified as

$$\begin{aligned} c_4(x,z) =& -\beta_i\beta_j r_x^2\,, \quad c_3(x,z) = -\delta_{i,j}\frac{r_x^2}{|x-z|} + \beta_i\beta_j\Big(\frac{4r_x r_z - 3r_x^2}{|x-z|}\Big)\,, \\ c_2(x,z) =& \delta_{i,j}\Big(\frac{2r_z^2}{|x-z|^2} - 2\Big) - \beta_i\beta_j\Big[k^2 r_x^2 + \frac{2r_z^2}{|x-z|^2}\Big]\,, \\ c_1(x,z) =& -\delta_{i,j}\Big[\frac{2r_z^2}{|x-z|^3} + \frac{k^2 r_x^2}{|x-z|}\Big] + \beta_i\beta_j\Big[\frac{2r_z^2}{|x-z|^3} + \frac{k^2 r_x^2}{|x-z|} - 2k^2 r_x\Big]\,. \end{aligned} \tag{3.42}$$

For the notational sake, we split the partial derivative of $F(x,z)$ in (3.36) into two parts such that $\frac{\partial^2 F(x,z)}{\partial x_i \partial z_j} = \delta_{i,j} g_1(x,z) + \beta_i\beta_j g_2(x,z)$, i.e., g_1 is the diagonal invariant part. Hence, for $\Xi_1^1(z,z)$ defined in (3.18), combining (3.35) and definitions of $g_1(x,z)$, $g_2(x,z)$, we have

$$(k^2\Xi_1^1(x,z))_{i,j} = 3\delta_{i,j} g_1(x,z) - \beta_i\beta_j g_2(x,z)\,. \tag{3.43}$$

To continue further, we write $r_d = r_x - r_z$, and $\mathbb{1}_{\{r_z - r_x\}} = 1$ for $r_z - r_x > 0$ and 0 otherwise. Then we derive

$$g_1(x,z) = 2\frac{\sin(kr_d) - kr_d\cos(kr_d)}{r_d^3} + 4r_x r_z \frac{(3-k^2r_d^2)\sin(kr_d) - 3kr_d\cos(kr_d)}{r_d^5},$$

$$g_2(x,z) = 2\frac{3kr_d\cos(kr_d) - (3-k^2r_d^2)\sin(kr_d)}{r_d^3} + 2(r_x^2 - r_x)\frac{kr_d(-k^2r_d^2+12)\cos(kr_d) + (5k^2r_d^2-12)\sin(kr_d)}{r_d^5}$$
$$+ 4r_x r_z \frac{3kr\cos(kr_d) - (3-k^2r_d^2)\sin(kr_d)}{r_d^5} - \mathbb{1}_{\{r_z - r_x\}} 4k^2 r_x \frac{\sin(kr_d) - kr_d\cos(kr_d)}{r_d^2}.$$

The denominator $n^1(z)$ defined in (3.22) can now be computed explicitly by choosing $x = z$ for both $g_1(x,z)$ and $g_2(x,z)$. This gives $g_1(z,z) = 2(2r_z^2k^5/15 + k^3/3)$ and $g_2(z,z) = -2k^5r_z^2/15 - 2k^5/15r_z$, implying

$$[\Xi_1^1(z,z)]_{i,j} = \delta_{i,j}\Big(\frac{4k^5}{5}r_z^2 + 2k^3\Big) + \beta_i\beta_j\Big(\frac{2k^5}{15}r_z^2 + \frac{2k^5}{15}r_z\Big),$$
$$n^1(z) = \Big|\sum \mathrm{diag}\{\Xi_1^1(z,z)\}\Big|^{\frac{1}{2}} = \Big|\frac{38k^5}{15}r_z^2 + \frac{2k^5}{15}r_z + 6k^3\Big|^{\frac{1}{2}}. \tag{3.44}$$

We observe that the normalization $n^1(z)$ is only a function of r_z and independent of (θ_z, ϕ_z). Hence, it has no influence towards our discussion in section 3.2.1 as we considered the desired mutually almost orthogonality properties for points with the same radial component in that subsection, i.e., with the same value for the normalization $n^1(z)$.

We now explain how $K^1_{\boldsymbol{c}_x,\boldsymbol{p}_z}(x,z)$ reaches a maximum at $z = x$ along the radial direction. From (3.43), since $\beta_i \le 1$ for $i = 1,2,3$, the coefficient associated with $g_1(x,z)$ is much larger than the coefficient associated with $g_2(x,z)$. Hence, we can now focus only on the diagonal invariant term, i.e., $g_1(x,z)$, and compute its second order Taylor expansion with respect to $r_d = r_x - r_z$ to derive

$$g_1(x,z) = \frac{2k^3}{3} - \frac{k^5r_d^2}{15} + r_x r_z\Big(\frac{4k^5}{15} - \frac{2k^7r_d^2}{105}\Big) + \mathcal{O}(r_d^4). \tag{3.45}$$

We observe that for both $2k^3/3 - k^5r_d^2/15$ and $4k^5/15 - 2k^7r_d^2/105$, they are second order polynomials that achieve the positive maximum at $r_d = r_x - r_z = 0$. However, the term r_xr_z for fixed r_x is undesired as it will shift the maximum point to the boundary when r_z is larger. Hence, a normalization term $n^1(z)$ of the order $\mathcal{O}(r_z)$, i.e. $|\sum \mathrm{diag}\{\Xi_1^1(z,z)\}|^{1/2}$ as in (3.44), is necessary to ensure that $K^{1,1}_{\boldsymbol{c}_x,\boldsymbol{p}_z}(x,z) = \boldsymbol{c}_x^T\,\Xi_1^1(x,z)\boldsymbol{p}_z/n^1(z)$ can achieve a maximum at $x \approx z$.

In Fig. 2, we examine the full version of the mutually almost orthogonality property between probing functions defined in (3.20) and Green's functions in (2.6) under $k = 5$. Two points $x_1 = (-0.45, -0.15, 0)$, $x_2 = (0.45, 0.05, 0)$ that are denoted by crosses in black represent the location of electric monopoles for plots in the first two columns, and the location of an electric monopole at x_2 and a magnetic monopole at x_1 for plots in the third column. The parameter γ is chosen as 1 for plots in the first two rows and as 3 for plots in the third row. The polarization direction $\boldsymbol{c}_x$ is selected as $(1,-1,1)^T/\sqrt{3}$ in all scenarios. The probing direction is chosen as $\boldsymbol{p}_z = \boldsymbol{c}_x$ for plots in the first row and as $\boldsymbol{p}_z = \boldsymbol{c}_x + 0.25(\epsilon_1,\epsilon_2,\epsilon_3)^T$, where $\epsilon_i \sim \mathcal{N}(0,1)$ for plots in the second and the third row. In each row, from left to right, we plot $K^{1,0}_{\boldsymbol{c}_{x_1},\boldsymbol{p}_z}(x_1,z) + K^{1,0}_{\boldsymbol{c}_{x_2},\boldsymbol{p}_z}(x_2,z)$, $K^{1,1}_{\boldsymbol{c}_{x_y},\boldsymbol{p}_z}(x_1,z) + K^{1,\gamma}_{\boldsymbol{c}_{x_2},\boldsymbol{p}_z}(x_2,z)$, $K^{2,\gamma}_{\boldsymbol{c}_{x_1},\boldsymbol{p}_z}(x_1,z) + K^{1,\gamma}_{\boldsymbol{c}_{x_2},\boldsymbol{p}_z}(x_2,z)$ as defined in (2.15) with respect to $z \in [-\sqrt{2},\sqrt{2}] \times [-\sqrt{2},\sqrt{2}] \times 0 \subset \Omega$. We have the following observations from Fig. 2:

- Comparing the first and second columns for kernel functions corresponding to probing functions in (3.7) and (3.20), the proposed new family of probing functions improves the sharpness of reconstruction significantly, i.e., successfully separates two electric monopoles that are close to each other.
- Looking at the third column for the case where an electric monopole and a magnetic monopole coexist in Ω, the magnitude of the kernel function $K^{1,\gamma}_{\boldsymbol{c}_x,\boldsymbol{p}_z}(x_2,z)$ is much larger than $K^{2,\gamma}_{\boldsymbol{c}_x,\boldsymbol{p}_z}(x_1,z)$, namely, it is not influenced by the existence of the magnetic monopole but the interaction between the measurement data and $\boldsymbol{w}_z^{1,\gamma}$ can help locate the electric monopole.
- Comparing the first and second rows for the case $\boldsymbol{p}_z = \boldsymbol{c}_x$ and $\boldsymbol{p}_z$ equals to $\boldsymbol{c}_x$ with 25% random perturbation, the desired mutually almost orthogonality property still holds with a very rough approximation to $\boldsymbol{c}_x$ that is the usual case in practice.
- Comparing the second column in the second and third rows for the cases $\gamma = 1, 3$, as γ increases, the reconstruction for the location of the electric monopole will be more accurate in the angular direction. Nonetheless, this improvement is only mild compared with the significant difference in the first and second columns for $\gamma = 0, 1$.

We conclude from the above analytical and numerical discussions that the family of probing functions $\boldsymbol{w}_z^{i,\gamma}$ $(i = 1,2)$ in (3.20) is a proper candidate to recover inhomogeneous inclusions of different types simultaneously with improved accuracy in the angular direction.

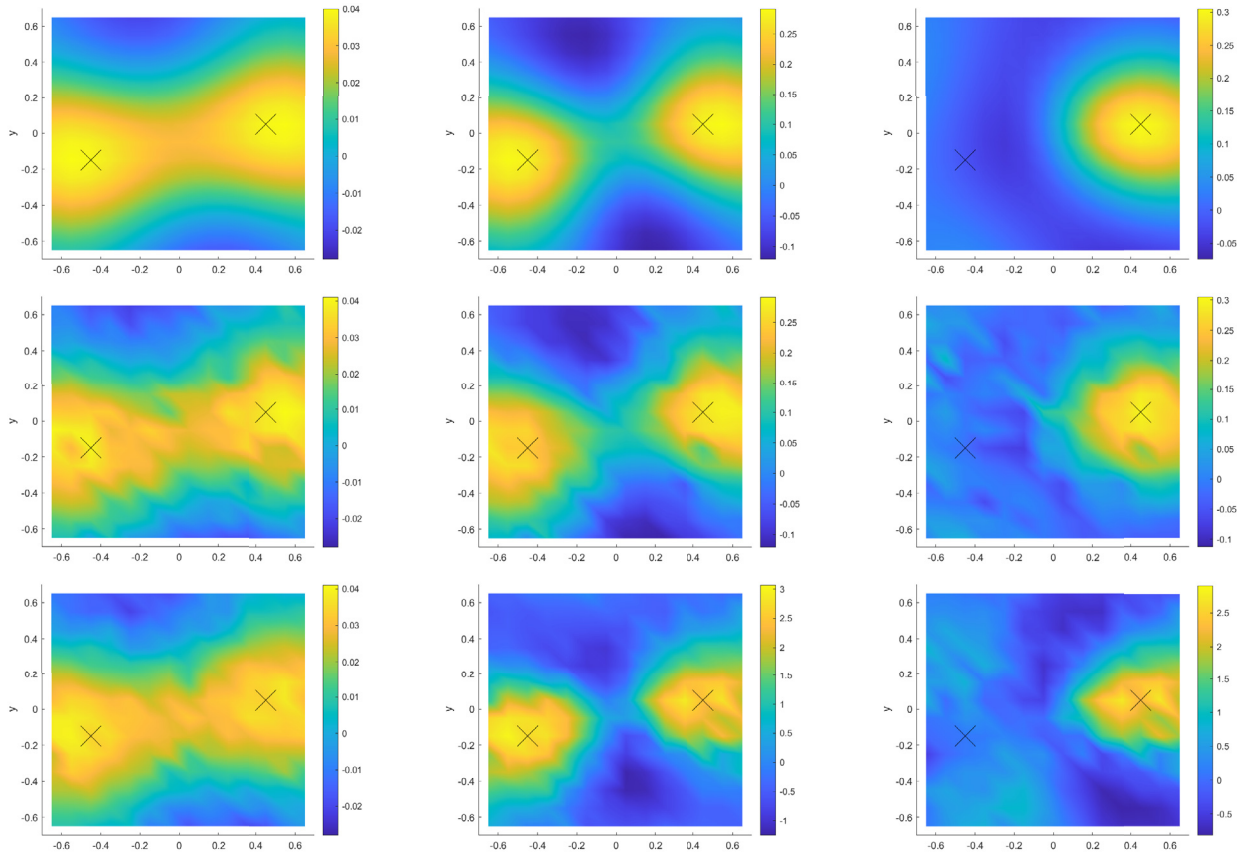

Fig. 2. In each row, from left to right: $K^{1,0}_{\boldsymbol{c}_{x_1},\boldsymbol{p}_z}(x_1,z)+K^{1,0}_{\boldsymbol{c}_{x_2},\boldsymbol{p}_z}(x_2,z)$, $K^{1,\gamma}_{\boldsymbol{c}_{x_\gamma},\boldsymbol{p}_z}(x_1,z)+K^{1,\gamma}_{\boldsymbol{c}_{x_2},\boldsymbol{p}_z}(x_2,z)$, $K^{2,\gamma}_{\boldsymbol{c}_{x_1},\boldsymbol{p}_z}(x_1,z)+K^{1,\gamma}_{\boldsymbol{c}_{x_2},\boldsymbol{p}_z}(x_2,z)$ (cf.(2.15)) with respect to $z\in[-\sqrt{2},\sqrt{2}]\times[-\sqrt{2},\sqrt{2}]\times 0$ under $\boldsymbol{c}_x=(1,-1,1)^T$, and $x_1=(-0.45,-0.15,0)$, $x_2=(0.45,0.05,0)$ (the crosses in black). For plots in the first row: $\gamma=1$, and $\boldsymbol{p}_z=\boldsymbol{c}_x$; for plots in the second row: $\gamma=1$ and $\boldsymbol{p}_z=\boldsymbol{c}_x+0.25(\epsilon_1,\epsilon_2,\epsilon_3)^T$ with $\epsilon_i\sim\mathcal{N}(0,1)$; for plots in the third row: $\gamma=3$, and $\boldsymbol{p}_z=\boldsymbol{c}_x+0.25(\epsilon_1,\epsilon_2,\epsilon_3)^T$ with $\epsilon_i\sim\mathcal{N}(0,1)$. (For interpretation of the colors in the figure(s), the reader is referred to the web version of this article.)

3.3. A family of probing functions that improves the accuracy of reconstruction in the radial direction

In the previous subsection, we proposed a family of probing functions that can induce kernel functions decaying fast in the angular direction but probably not in the radial direction. We now construct another family of probing functions that induce kernel functions being able to decay fast in the radial direction, which can be used either independently or simultaneously with the family of probing functions (3.20).

We first present a closed form of the kernel functions with undetermined radial components. It will be clear from the closed form that the Fourier transform of the kernel function in the radial direction is related to the Fourier transform of the radial component of the probing function. Then we may choose a proper probing function such that the kernel function can approximate a sharp Gaussian kernel, i.e., $\exp(-\lambda|r_x-r_z|^2)$ for $\lambda>0$ in the radial direction with respect to the L^2 norm. The mutually almost orthogonality properties are then verified through numerical experiments.

We recall our discussions in section 3.2 that a probing function of the form (3.20) possesses the mutually almost orthogonality property in the angular direction with different choices of γ. Hence, we shall assume the new family of probing functions have the same angular component as in (3.20) but different radial components to be determined, i.e.,

$$\boldsymbol{w}_z^{1,R}(y)=\sum_{m,n}\Big[\big(g_2^n(kr_z)A_{2,m,n}(z)+g_3^n(kr_z)A_{3,m,n}(z)\big)\big(\boldsymbol{u}^\dagger_{1,m,n}(y)+c_{4,n}\boldsymbol{u}^\dagger_{4,m,n}(y)\big) + g_1^n(kr_z)A_{1,m,n}(z)\big(\boldsymbol{u}^\dagger_{2,m,n}(y)+c_{3,n}\boldsymbol{u}^\dagger_{3,m,n}(y)\big)\Big], \tag{3.46}$$

$$\boldsymbol{w}_z^{2,R}(y)=\sum_{m,n}\Big[g_1^n(kr_z)A_{1,m,n}(z)\big(\boldsymbol{u}^\dagger_{1,m,n}(y)+c_{4,n}\boldsymbol{u}^\dagger_{4,m,n}(y)\big) + \big(g_2^n(kr_z)A_{2,m,n}(z)+g_3^n(kr_z)A_{3,m,n}(z)\big)\big(\boldsymbol{u}^\dagger_{2,m,n}(y)+c_{3,n}\boldsymbol{u}^\dagger_{3,m,n}(y)\big)\Big] \tag{3.47}$$

for $z \in \Omega$, where g_i^n $(i = 1, 2, 3)$ will be determined later so that the resulting DSM is also accurate in reconstructing the location of inhomogeneous inclusions in the radial direction.

For the notational sake, we define an auxiliary matrix valued function:

$$\Xi_1^R(x,z) := \sum_{m,n} \frac{2n+1}{4\pi}\Big[\boldsymbol{v}_{2,m,n}(x)(g_2^n(kr_z)A_{2,m,n}^\dagger(z) + g_3^n(kr_z)A_{3,m,n}^\dagger(z)) + \boldsymbol{v}_{1,m,n}(x)g_1^n(kr_z)A_{1,m,n}^\dagger(z)\Big], \tag{3.48}$$

then we have (without the normalization term as in (2.14))

$$K_{\boldsymbol{c}_x,\boldsymbol{p}_z}^{1,R}(x,z) = \boldsymbol{c}_x^T\,\Xi_1^R(x,z)\boldsymbol{p}_z = \langle \nu \times (\Phi_x \cdot \boldsymbol{c}_x)\,,\ \boldsymbol{w}_z^{1,R}\cdot\boldsymbol{p}_z\rangle_{L^2(\partial\Omega)} = \langle \nu \times (\nabla \times \Phi_x \cdot \boldsymbol{c}_x)\,,\ \boldsymbol{w}_z^{2,R}\cdot\boldsymbol{p}_z\rangle_{L^2(\partial\Omega)}\,. \tag{3.49}$$

We now focus on the first characteristic of the mutually almost orthogonality property, i.e., $K_{\boldsymbol{c}_x,\boldsymbol{p}_z}^{1,R}(x,z)$ achieves the maximum when $z \approx x$ by requiring it approximates a Gaussian kernel for any directions $\boldsymbol{d}$, and the second characteristic regarding the decoupling effect will be verified numerically later; see Fig. 3. To determine the numerical value of $g_i^n(kr_z)$, we use the definition in (3.48) and recall the derivation of the expansion of Ξ_1^γ in section 3.2.1 and $f_{i,x}^n$ in (3.25) to get

$$\begin{aligned}\boldsymbol{d}^T\,\Xi_1^R(x,z)\boldsymbol{d} = \sum_n \frac{2n+1}{4\pi}\Big[&f_{3,x}^n g_3^n h_{3,3}^n(\hat{x},\hat{z},\boldsymbol{d}) + \frac{f_{2,x}^n g_2^n}{n^2+n}h_{2,2}^n(\hat{x},\hat{z},\boldsymbol{d}) \\ &+ \frac{f_{1,x}^n g_1^n}{n^2+n}h_{1,1}^n(\hat{x},\hat{z},\boldsymbol{d}) + \frac{f_{3,x}^n g_2^n h_{3,2}^n(\hat{x},\hat{z},\boldsymbol{d}) + f_{2,x}^n g_3^n h_{2,3}^n(\hat{x},\hat{z},\boldsymbol{d})}{\sqrt{n^2+n}}\Big],\end{aligned} \tag{3.50}$$

with $t = \hat{x}\cdot\hat{z}$ and $\boldsymbol{d} = d_r^x\hat{\boldsymbol{r}}_x + d_\theta^x\hat{\boldsymbol{\theta}}_x + d_\phi^x\hat{\boldsymbol{\phi}}_x$, and

$$\begin{aligned}
h_{3,3}^n(\hat{x},\hat{z},\boldsymbol{d}) &= d_r^x d_r^z P_n(t)\,,\\
h_{2,2}^n(\hat{x},\hat{z},\boldsymbol{d}) &= \frac{d_\phi^x d_\phi^z}{\sin\theta_x\sin\theta_z}\Big[\frac{\partial^2 t}{\partial\phi_x\partial\phi_z}\frac{-P_n^1(t)}{\sqrt{1-t^2}} + \frac{\partial t}{\partial\phi_x}\frac{\partial t}{\partial\phi_z}\frac{P_n^2(t)}{1-t^2}\Big] + d_\theta^x d_\theta^z\Big[\frac{\partial^2 t}{\partial\theta_x\partial\theta_z}\frac{-P_n^1(t)}{\sqrt{1-t^2}} + \frac{\partial t}{\partial\theta_x}\frac{\partial t}{\partial\theta_z}\frac{P_n^2(t)}{1-t^2}\Big]\\
&\quad + \Big[\frac{d_\theta^x d_\phi^z}{\sin\theta_z}\frac{\partial t}{\partial\phi_z}\frac{\partial t}{\partial\theta_x} + \frac{d_\phi^x d_\theta^z}{\sin\theta_x}\frac{\partial t}{\partial\phi_x}\frac{\partial t}{\partial\theta_z}\Big]\frac{P_n^2(t)}{1-t^2} - \Big[\frac{d_\theta^x d_\phi^z}{\sin\theta_z}\frac{\partial^2 t}{\partial\phi_z\partial\theta_x} + \frac{d_\phi^x d_\theta^z}{\sin\theta_x}\frac{\partial^2 t}{\partial\phi_x\partial\theta_z}\Big]\frac{P_n^1(t)}{\sqrt{1-t^2}}\,,\\
h_{1,1}^n(\hat{x},\hat{z},\boldsymbol{d}) &= \frac{d_\theta^x d_\theta^z}{\sin\theta_x\sin\theta_z}\Big[\frac{\partial^2 t}{\partial\phi_x\partial\phi_z}\frac{-P_n^1(t)}{\sqrt{1-t^2}} + \frac{\partial t}{\partial\phi_x}\frac{\partial t}{\partial\phi_z}\frac{P_n^2(t)}{1-t^2}\Big] + d_\phi^x d_\phi^z\Big[\frac{\partial^2 t}{\partial\theta_x\partial\theta_z}\frac{-P_n^1(t)}{\sqrt{1-t^2}} + \frac{\partial t}{\partial\theta_x}\frac{\partial t}{\partial\theta_z}\frac{P_n^2(t)}{1-t^2}\Big]\\
&\quad - \Big[\frac{d_\phi^x d_\theta^z}{\sin\theta_z}\frac{\partial t}{\partial\phi_z}\frac{\partial t}{\partial\theta_x} + \frac{d_\theta^x d_\phi^z}{\sin\theta_x}\frac{\partial t}{\partial\phi_x}\frac{\partial t}{\partial\theta_z}\Big]\frac{P_n^2(t)}{1-t^2} + \Big[\frac{d_\phi^x d_\theta^z}{\sin\theta_z}\frac{\partial^2 t}{\partial\phi_z\partial\theta_x} + \frac{d_\theta^x d_\phi^z}{\sin\theta_x}\frac{\partial^2 t}{\partial\phi_x\partial\theta_z}\Big]\frac{P_n^1(t)}{\sqrt{1-t^2}}\,,\\
h_{3,2}^n(\hat{x},\hat{z},\boldsymbol{d}) &= \Big[d_r^x d_\theta^z\frac{\partial t}{\partial\theta_x} + \frac{d_r^x d_\phi^z}{\sin\theta_x}\frac{\partial t}{\partial\phi_x}\Big]\frac{(-P_n^1(t))}{\sqrt{1-t^2}}\,,\quad h_{2,3}(\hat{x},\hat{z},\boldsymbol{d}) = \Big[d_\theta^x d_r^z\frac{\partial t}{\partial\theta_z} + \frac{d_\phi^x d_r^z}{\sin\theta_z}\frac{\partial t}{\partial\phi_z}\Big]\frac{(-P_n^1(t))}{\sqrt{1-t^2}}\,.
\end{aligned}$$

Since we are interested in this section in constructing a family of probing functions that can induce kernel functions that decay very fast in the radial direction, we first focus on the case $\hat{x} = \hat{z}$. Similarly to the simplification in (3.26), using specific values of the Legendre polynomial, $\boldsymbol{d}^T\,\Xi_1^R(x,z)\boldsymbol{d}$ becomes

$$\begin{aligned}&\boldsymbol{d}^T\,\Xi_1^R(x,z)\boldsymbol{d} \\ &= \sum_n \frac{2n+1}{4\pi}\Big[(n^2+n)f_3^n(kr_x)g_3^n(kr_z)d_r^x d_r^z + \Big(\frac{f_1^n(kr_x)g_1^n(kr_z)}{2} + \frac{f_2^n(kr_x)g_2^n(kr_z)}{2}\Big)\Big(d_\theta^x d_\theta^z + d_\phi^x d_\phi^z\Big)\Big].\end{aligned} \tag{3.51}$$

We see from (3.51) that there are no interaction terms among $g_i^n(kr_z)$ for $i = 1, 2, 3$. Hence, if we can compute g_i^n such that $\sum_n c_n g_i^n(kr_z)f_i^n(kr_x) \approx \exp(-\lambda|r_x - r_z|^2)$ for each i, then $\boldsymbol{d}^T\,\Xi_1^R(x,z)\boldsymbol{d}$ will approximate $\exp(-\lambda|r_x - r_z|^2)$ for every direction $\boldsymbol{d}$.

To approximate a Gaussian kernel, for a fixed r_z, we first observe that the convolution of $j_0(kr_x)$ with general $g_{r_z} \in L^2(\mathbb{R})$ can be written as

$$\begin{aligned}&\int_{\mathbb{R}} j_0(k|r_x - r_y|)g_{r_z}(r_y)dr_y \approx \sum_j j_0(k|r_x - r_{y_j}|)g_{r_z}(r_{y_j})h = \sum_n h\frac{2n+1}{k}j_n(kr_x)\sum_{y_j}\big[j_n(kr_{y_j})g_{r_z}(r_{y_j})\big]\\
&= \sum_n j_n(kr_x)g_1^n(kr_z)\,,\ \text{with } g_1^n(kr_z) = h(2n+1)/k\sum_{y_j}\big[j_n(kr_{y_j})g_{r_z}(r_{y_j})\big],\end{aligned} \tag{3.52}$$

where we have used $j_0(k|x-y|) = \sum_n (2n+1)/kj_n(kx)j_n(ky)$, $f_1^n(kr_x) = j_n(kr_x)$, and $h := r_{y_{j+1}} - r_{y_j}$ for all j. From the above equation, the sum $\sum_n j_n(kr_x)g_1^n(kr_z)$ can be used to approximate the convolution between j_0 and g_{r_z}. We remark

that all infinite sums can be truncated to a finite sum with desired accuracy since $j_n(kr)$ decays exponentially with respect to n for fixed r.

To achieve the almost orthogonality property, we know from (3.52) that it suffices to require $\int_{\mathbb{R}} j_0(k|r_x - r_y|)g_{r_z}(r_y)dr_y$ to approximate $\exp(-\lambda|r_x - r_z|^2)$. We recall the Fourier transform of j_0 and the Gaussian kernel:

$$\int_{\mathbb{R}} j_0(k|r_x|)\exp(-i\omega r_x)dr_x = \frac{\pi}{2}\big[\text{sign}(\omega - k) - \text{sign}(\omega + k)\big]; \tag{3.53}$$

$$\int_{\mathbb{R}} \exp(-\lambda|r_z - r_x|^2)\exp(-i\omega r_x)dr_x = \exp(-i\omega r_z)\sqrt{\frac{\pi}{\lambda}}\exp\big(-\frac{\omega^2}{4\lambda}\big). \tag{3.54}$$

To determine g_1^n, as the Fourier transform of $j_0(k|r_x|)$ is band-limited, the best approximation to the Gaussian kernel by (3.52) is given by

$$\min_{g\in L^2(\mathbb{R})}\Big|\Big|\sum_n j_n(kr_x)g_1^n(kr_z) - \exp(-\lambda|r_x - r_z|^2)\Big|\Big|_{L^2(\mathbb{R})} = \frac{2\pi}{\lambda}\int_k^\infty \exp\big(-\frac{\omega^2}{2\lambda}\big)d\omega\,. \tag{3.55}$$

From this expression, we observe that the function $\sum_n j_n(kr_x)g_1^n(kr_z)$ can approximate a Gaussian kernel with a relatively small error along the radial direction and the error can be obtained from the specific value of the cumulative distribution function associated with the normal distribution.

Hence, to achieve the almost orthogonality property, we may expect two important and reasonable requirements on the kernel function that are used for the following numerical computation of the probing functions:

1. When $\hat{x} = \hat{z}$, we like the coefficients of $\boldsymbol{d}^T\Xi_1^R(x,z)\boldsymbol{d}$ in (3.51) are approximately to be a Gaussian kernel, i.e., $\sum_n f_i^n(kr_x)g_i^n(kr_z)$ to be $\exp(-\lambda|r_x - r_z|^2)$ approximately for $i = 1, 2, 3$;
2. When $\hat{x} \neq \hat{z}$, we like the coefficients of $\boldsymbol{d}^T\Xi_1^R(x,z)\boldsymbol{d}$ in (3.51) are small for any x and z.

In the following, we will solve a minimization problem to determine the numerical value of the probing function. With the help of our analysis on the kernel function in (3.50) and (3.51), the computation can be simplified. We remark that g_2^n and g_3^n can be computed in a similar manner as the above.

Computing the probing functions. In the numerical implementation of DSM, we need to compute the probing functions in a discretized setting. Consider a set of nodal points in the radial direction $\boldsymbol{r}_b = \{r_\beta | 0 < r_\beta < 1,\ 1 \le \beta \le b\}$, a set of points on the sphere $T = \{(\theta_\tau, \phi_\tau) | 1 \le \tau \le t\} \subset \mathbb{S}^2$, a set of points in the sampling domain as $\boldsymbol{z}_\tau = \{z_{\tau,\beta} = (r_\beta, \theta_\tau, \phi_\tau) | r_\beta \in \boldsymbol{r}_b\,,\ (\theta_\tau, \phi_\tau) \in T\}$, and three choices of directions $\boldsymbol{d} = \boldsymbol{e}_1, \boldsymbol{e}_2, \boldsymbol{e}_3$, which are basis vectors in $\mathbb{R}^3$. We remark that the set T and $\boldsymbol{z}_\tau$ are used to achieve the almost orthogonality property when $\hat{x} \neq \hat{z}$. From our numerical experiments, we observe that two points, that is (θ_τ, ϕ_τ), on the sphere are already satisfactory to ensure the kernel function introduced in (3.49) reaches the maximum at $z \approx x$ in the angular direction, which are $(\theta_x + \pi, \phi_x)$ and $(\theta_x + \pi/2, \phi_x)$. Denoting

$$G_i = \begin{pmatrix} g_i^0(kr_1) & g_i^1(kr_1) & \cdots & g_i^N(kr_1) \\ g_i^0(kr_2) & \ddots & & g_i^N(kr_2) \\ \vdots & & \ddots & \vdots \\ g_i^0(kr_b) & g_i^1(kr_b) & \cdots & g_i^N(kr_b) \end{pmatrix}, \quad F_i = \begin{pmatrix} f_i^0(kr_1) & f_i^1(kr_1) & \cdots & f_i^N(kr_1) \\ f_i^0(kr_2) & \ddots & & f_i^N(r_2) \\ \vdots & & \ddots & \vdots \\ f_i^0(kr_b) & f_i^1(kr_b) & \cdots & f_i^N(kr_b) \end{pmatrix}, \tag{3.56}$$

then the first requirement after equation (3.55) can be reformulated as finding G_i such that $F_1G_1^T \approx \boldsymbol{L}_b$ where $\boldsymbol{L}_b$ is the $b \times b$ discretization matrix for $\exp(-\lambda|r_x - r_z|^2)$ for r_x and $r_z \in (0, 1)$. We choose $\lambda = 3k$ in numerical experiments.

For the second requirement after equation (3.55), we write

$$H_{1,1}^{\boldsymbol{d},\tau} = \begin{pmatrix} h_{1,1}^0(\hat{x}_0, \hat{z}_{\tau,1}, \boldsymbol{d}) & h_{1,1}^1(\hat{x}_0, \hat{z}_{\tau,1}, \boldsymbol{d}) & \cdots & h_{1,1}^N(\hat{x}_0, \hat{z}_{\tau,1}, \boldsymbol{d}) \\ h_{1,1}^0(\hat{x}_0, \hat{z}_{\tau,2}, \boldsymbol{d}) & \ddots & & h_{1,1}^N(\hat{x}_0, \hat{z}_{\tau,2}, \boldsymbol{d}) \\ \vdots & & \ddots & \vdots \\ h_{1,1}^0(\hat{x}_0, \hat{z}_{\tau,b}, \boldsymbol{d}) & h_{1,1}^1(\hat{x}_0, \hat{z}_{\tau,b}, \boldsymbol{d}) & \cdots & h_{1,1}^N(\hat{x}_0, \hat{z}_{\tau,b}, \boldsymbol{d}) \end{pmatrix}, \quad \Gamma_2 = \text{diag}\Big\{\frac{2n+1}{4\pi(n^2+n)}\Big\}. \tag{3.57}$$

Then the second requirement for g_1^n above can be reformulated as finding G_1 such that $||F_1H_{1,1}^{\boldsymbol{d}}\Gamma_2G_1^T||_2$ is small.

Combining the above requirements, we can solve G_1, i.e., numerical values of $g_1^n(kr_z)$ for $0 \le n \le N$ and $r_z \in \boldsymbol{r}_b$, by solving

$$\min_{G_1}\Big|\Big|F_1\begin{pmatrix}\Gamma_1 & H_1\Gamma_2 & H_2\Gamma_2\end{pmatrix}^T G_1^T - \begin{pmatrix}\boldsymbol{L}_b & \boldsymbol{0}_{b,b} & \boldsymbol{0}_{b,b}\end{pmatrix}^T\Big|\Big|_2, \tag{3.58}$$

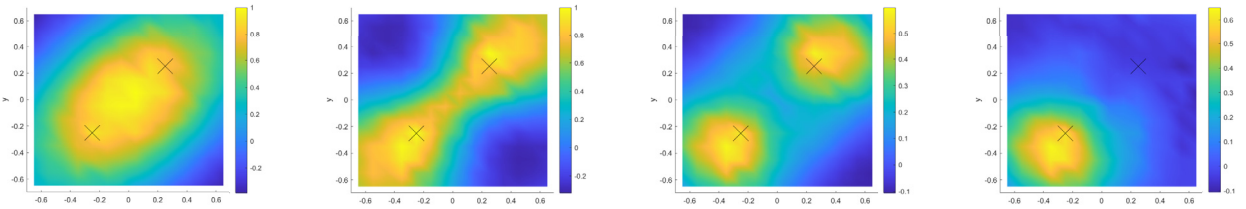

Fig. 3. From left to right: $K^{1,0}_{\boldsymbol{c}_{x_1},\boldsymbol{p}_z}(x_1,z)+K^{1,0}_{\boldsymbol{c}_{x_2},\boldsymbol{p}_z}(x_2,z)$, $K^{1,2}_{\boldsymbol{c}_{x_1},\boldsymbol{p}_z}(x_1,z)+K^{1,2}_{\boldsymbol{c}_{x_2},\boldsymbol{p}_z}(x_2,z)$, $K^{1,R}_{\boldsymbol{c}_{x_1},\boldsymbol{p}_z}(x_1,z)+K^{1,R}_{\boldsymbol{c}_{x_2},\boldsymbol{p}_z}(x_2,z)$, and $K^{2,R}_{\boldsymbol{c}_{x_1},\boldsymbol{p}_z}(x_1,z)+K^{1,R}_{\boldsymbol{c}_{x_2},\boldsymbol{p}_z}(x_2,z)$ induced by probing functions defined in (3.7), (3.20), and (3.46) with respect to $z\in[-\sqrt{2},\sqrt{2}]\times[-\sqrt{2},\sqrt{2}]\times 0$ under $k=4$, and $x_1=(0.25,0.25,0)$, $x_2=(-0.25,-0.25,0)$ which are denoted by crosses in black. Directions are $\boldsymbol{c}_x=(1,1,-1)^T/\sqrt{3}$, $\boldsymbol{p}_z=\boldsymbol{c}_x+0.1(\epsilon_1,\epsilon_2,\epsilon_3)^T$, with $\epsilon_i\sim\mathcal{N}(0,1)$.

where $H_j=(H^{\boldsymbol{e}_1,j}_{1,1}, H^{\boldsymbol{e}_2,j}_{1,1}, H^{\boldsymbol{e}_3,j}_{1,1})$ and $\mathbf{0}_{b,b}$ is the $b\times b$ zero matrix. The minimization problem can be solved by using the pseudo-inverse of $(F_1, F_1H_1\Gamma_2, F_1H_2\Gamma_2)^T$. We remark that the j^{th} column of G_1^T which represents the radial component of probing functions for sampling points z with $r_z=r_{z_j}$ is given by the j^{th} column of $[(F_1, F_1H_1\Gamma_2, F_1H_2\Gamma_2)^T]^\dagger$. The value of $g^n_2(kr_\tau)$ and $g^n_3(kr_\tau)$ can be computed similarly.

We remark that the singular value decomposition (SVD) may be used for the computation of the pseudo-inverse for solving (3.58), but this can be conducted offline.

Numerical verification of the mutually almost orthogonality property. We numerically examine the mutually almost orthogonality property between probing functions proposed in this subsection and Green's functions; see Fig. 3. For simplicity, we write $K^{i,R}_{\boldsymbol{d},\boldsymbol{p}}(x,z)$ similarly as in (2.15) with probing functions constructed in (3.46). We consider the case $k=4$ with $\boldsymbol{c}_x=(1,1,-1)^T/\sqrt{3}$, $\boldsymbol{p}_z=\boldsymbol{c}_x+0.05(\epsilon_1,\epsilon_2,\epsilon_3)^T$, where $\epsilon_i\sim\mathcal{N}(0,1)$ for $i=1,2,3$. For $x_1=(0.25,0.25,0)$, $x_2=(-0.25,-0.25,0)$ denoted by crosses in black, two electric monopoles are located at both x_1 and x_2 for the first three plots; and one electric monopole is located at x_1, one magnetic monopole is located at x_2 for the fourth plot. The minimization problem (3.58) is solved by using the truncated singular value decomposition for the first six singular values. From left to right, we plot $K^{1,0}_{\boldsymbol{c}_{x_1},\boldsymbol{p}_z}(x_1,z)+K^{1,0}_{\boldsymbol{c}_{x_2},\boldsymbol{p}_z}(x_2,z)$, $K^{1,2}_{\boldsymbol{c}_{x_1},\boldsymbol{p}_z}(x_1,z)+K^{1,2}_{\boldsymbol{c}_{x_2},\boldsymbol{p}_z}(x_2,z)$, $K^{1,R}_{\boldsymbol{c}_{x_1},\boldsymbol{p}_z}(x_1,z)+K^{1,R}_{\boldsymbol{c}_{x_2},\boldsymbol{p}_z}(x_2,z)$, and $K^{2,R}_{\boldsymbol{c}_{x_1},\boldsymbol{p}_z}(x_1,z)+K^{1,R}_{\boldsymbol{c}_{x_2},\boldsymbol{p}_z}(x_2,z)$ induced by probing functions defined in (3.7), (3.20), and (3.46) respectively with respect to $z\in[-\sqrt{2},\sqrt{2}]\times[-\sqrt{2},\sqrt{2}]\times 0\subset\Omega$. We observe from Fig. 3 the following:

- Comparing the first three plots for the kernel functions corresponding to the probing functions defined in (3.7), (3.20) and (3.46), respectively, $K^{1,R}_{\boldsymbol{c}_x,\boldsymbol{p}_z}(x,z)$ in the third plot induced by $\boldsymbol{w}^{1,R}_z$ proposed in this subsection is the only kernel function that can well separate the two electric monopoles at x_1, x_2 due to the improved sharpness in the radial direction.
- Looking at the fourth plot, for the case that an electric monopole at x_2 and a magnetic monopole at x_1 coexist in the domain, it is important to note that the interaction between the measurement data and $\boldsymbol{w}^{1,R}_z$ can help locate the electric monopole and the result is not influenced by the existence of the magnetic monopole.

Hence, we conclude that the family of probing functions $\boldsymbol{w}^{i,R}_z$ for $i=1,2$ in (3.46) is an appropriate candidate to recover inhomogeneous inclusions of different type simultaneously with improved accuracy in radial direction.

To summarize, for probing functions defined in (3.46), the corresponding index functions in (2.14) for recovering the inhomogeneous inclusions Ω_ϵ and Ω_μ are defined as (without the normalization term):

$$I^R_{mo}(z):=\langle \nu\times E^s,\ \boldsymbol{w}^{1,R}_z\cdot\boldsymbol{p}_z\rangle_{L^2(\partial\Omega)},\quad I^R_{di}(z):=\langle \nu\times E^s,\ \boldsymbol{w}^{2,R}_z\cdot\boldsymbol{q}_z\rangle_{L^2(\partial\Omega)}. \tag{3.59}$$

We remark that, in the current work, we are primarily focused on the cases when there are very limited observation data available, e.g., the measurement data from only one or two incident fields with the same frequency. When the measurement data is available at multiply frequencies, some special strategy, e.g., similar to the one in the paper [25], might be considered to improve the accuracy of the reconstruction of the DSM by combining the index functions of several frequencies together in some appropriate manner.

We conclude this section with one remark about the probing directions that we should choose in real applications for index functions appeared in (3.22) and (3.59). Our discussions in this section suggest us to choose $\boldsymbol{p}_z\approx\boldsymbol{c}_x$ and $\boldsymbol{q}_z\approx\boldsymbol{d}_x$, where $\boldsymbol{c}_x$ and $\boldsymbol{d}_z$ are defined in (2.13). From the derivation of (2.13), we know that $\boldsymbol{c}_x$ and $\boldsymbol{d}_x$ can be taken to be about the same vector as $E(x)$ and $\nabla\times E(x)$, respectively, for all $x\in\Omega$, if the inhomogeneous inclusions are isotropic. For the case that the incident field is known as we consider in this section, we see from the above numerical experiments that the desired mutually almost orthogonality properties hold when the probing directions are taken to be very rough approximations of $E(z)$ and $\nabla\times E(z)$. For example, we have chosen $\boldsymbol{p}_z=\boldsymbol{c}_x+\delta(\epsilon_1,\epsilon_2,\epsilon_3)^T$, with $\epsilon_i\sim\mathcal{N}(0,1)$ and $\delta\geq 0.1$, in Figs. 2 and 3. Hence, when the incident field E^i is explicitly available as the discussion in this section, we would suggest to employ it as appropriate approximations, i.e., choosing $\boldsymbol{p}_z=E^i(z)$ and $\boldsymbol{q}_z=\nabla\times E^i(z)$.

4. Recovering inhomogeneous inclusions with no prior knowledge of the incident field

In this section, we consider the inverse problem of recovering the support of inhomogeneous inclusions from a pair of boundary measurements for both the electric and magnetic fields, with no prior knowledge of the incident field in $\mathbb{R}^3$. All the notations are carried over from the previous sections.

In terms of the electric field, our problem is stated as follows: for a fixed k and E that satisfies

$$\nabla \times (\mu^{-1}\nabla \times E) - k^2 \epsilon E = 0 \text{ in } \Omega\,, \tag{4.1}$$

we aim to recover the inhomogeneous inclusions Ω_μ=supp$\{\mu-\mu_0\}$ and Ω_ϵ=supp$\{\epsilon-\epsilon_0\}$ simultaneously, when only one or two pairs of measurements $\nu \times E$ and $\nu \times \nabla \times E$ is available on the boundary $\partial\Omega$. We know from the Maxwell theory that $\nu \times \nabla \times E$ is basically the tangential component of the magnetic field. The uniqueness and stability of the reconstruction for this inverse problem can be found in [8,11]. Let E_0 be the electric field associated with the homogeneous background, satisfying

$$\nabla \times \nabla \times E_0 - k^2 E_0 = 0 \quad \text{in } \Omega\,. \tag{4.2}$$

We shall write $E_s := E - E_0$ in the sequel, and can easily see that it satisfies

$$\nabla \times \nabla \times E_s - k^2 E_s = k^2(\epsilon-\epsilon_0)E - \nabla \times \Big(\frac{1}{\mu} - \frac{1}{\mu_0}\Big)\nabla \times E \text{ in } \Omega\,. \tag{4.3}$$

Similarly to our derivations in section 2 (see equations (2.9)-(2.13)), we can represent the measurement on the boundary with Green's function and its curl. To achieve that, we introduce the Green's function of the second kind, denoted by Ψ_x, satisfying

$$\nabla \times \nabla \times \Psi_x(y) - k^2 \Psi_x(y) = \delta_x(y)\boldsymbol{I}_3 \text{ in } \Omega\,, \qquad \nu \times \nabla \times \Psi_x(y) = 0 \text{ on } \partial\Omega\,. \tag{4.4}$$

Using the Green's representation formula, we derive [4]

$$\begin{aligned} E_s(x) &= \int_\Omega \Psi_x\Big[k^2(\epsilon-\epsilon_0)E - \nabla \times \Big(\frac{1}{\mu} - \frac{1}{\mu_0}\Big)\nabla \times E\Big]dz \\ &= \int_{\Omega_\epsilon} k^2(\epsilon-\epsilon_0)\Psi_x E dz - \int_{\Omega_\mu} \Big(\frac{1}{\mu} - \frac{1}{\mu_0}\Big)(\nabla_z \times \Psi_x)(\nabla \times E)dz + \int_{\partial\Omega_\mu} \Big(\frac{1}{\mu} - \frac{1}{\mu_0}\Big)(\nabla \times \Psi_x)(\nu \times E)ds(z)\,, \end{aligned} \tag{4.5}$$

when μ is piecewise constant. From (4.5), an appropriate numerical integration approximation leads to

$$E_s(x) \approx \sum_i a_i(\Psi_{y_i}(x)\cdot \boldsymbol{c}_i) + \sum_j b_j(\nabla_z \times \Psi_{z_j}(x)\cdot \boldsymbol{d}_j)\,, \quad x \in \partial\Omega\,,\ y_i \in \Omega_\epsilon\,,\ z_j \in \Omega_\mu\,, \tag{4.6}$$

where a_i, $b_j \in \mathbb{C}$, and $\boldsymbol{c}_i$, $\boldsymbol{d}_j \in \mathbb{C}^3$.

For the reconstruction with respect to (4.1), all the definitions of index functions and kernel functions in section 2 are carried over here. The remaining task is to construct a proper family of probing functions, $\tilde{\boldsymbol{w}}_z^1$ and $\tilde{\boldsymbol{w}}_z^2$, for recovering Ω_ϵ and Ω_μ.

We continue the discussions by considering the typical measurement surface $\partial\Omega = \mathbb{S}^2$. Firstly, we will represent the Green's function of the second kind by spherical vector waves. We notice that one particular solution for (4.4) can be constructed by $\Psi_x(y) = \Phi_x(y) + \widetilde{\Psi}_x(y)$ where $\Phi_x(y)$ is the free space Green's function in (2.6) and $\widetilde{\Psi}_x(y)$ satisfies

$$\nabla \times \nabla \times \widetilde{\Psi}_x(y) - k^2 \widetilde{\Psi}_x(y) = 0 \text{ in } \Omega\,, \qquad \nu \times \nabla \times \widetilde{\Psi}_x(y) = \nu \times \nabla \times \Phi_x(y) \text{ on } \partial\Omega\,. \tag{4.7}$$

Combining the expansion in (3.1) and orthogonality properties of spherical vector waves in (A.10), we have

$$\Psi_x(y) = ik\sum_{m,n}\Big[\boldsymbol{v}_{1,m,n}(x)\big(b_n \boldsymbol{v}^\dagger_{1,m,n}(y) + \boldsymbol{u}^\dagger_{1,m,n}(y)\big) + \boldsymbol{v}_{2,m,n}(x)\big(a_n \boldsymbol{v}^\dagger_{2,m,n}(y) + \boldsymbol{u}^\dagger_{2,m,n}(y)\big)\Big]\,, \tag{4.8}$$

where the coefficients a_n and b_n can be determined by using the boundary condition $\nu \times \nabla \times \widetilde{\Psi}_x(y) = \nu \times \nabla \times \Phi_x(y)$ on $\mathbb{S}^2$, and are given by

$$a_n = -\frac{h_n^{(1)}(k)}{j_n(k)}\,, \quad b_n = -\frac{(d/d\rho)[\rho h_n^{(1)}(\rho)]}{(d/d\rho)[\rho\, j_n(\rho)]}\Big|_{\rho=k}\,, \tag{4.9}$$

with $h_n^{(1)}$ being the spherical Bessel function of the first kind of order n.

Similarly, the curl field can be expressed as

$$\nabla_x \times \Psi_x(y) = ik^2 \sum_{m,n} \Big[\boldsymbol{v}_{2,m,n}(x)\big(b_n \boldsymbol{v}^{\dagger}_{1,m,n}(y) + \boldsymbol{u}^{\dagger}_{1,m,n}(y)\big) + \boldsymbol{v}_{1,m,n}(x)\big(a_n \boldsymbol{v}^{\dagger}_{2,m,n}(y) + \boldsymbol{u}^{\dagger}_{2,m,n}(y)\big)\Big]. \tag{4.10}$$

To design a set of proper probing functions, we follow the similar idea as in section 3, i.e., to choose probing functions that can induce certain kernel functions that we desire. For the convenience of the following discussions, as in (3.5), we first compute a set of coefficients $d_{3,n}$ and $d_{4,n}$ which satisfy

$$\langle \nu \times \big(a_n \boldsymbol{v}^{\dagger}_{2,m,n} + \boldsymbol{u}^{\dagger}_{2,m,n}\big),\ \boldsymbol{u}^{\dagger}_{1,m',n'} + d_{4,n'} \boldsymbol{u}^{\dagger}_{4,m',n'} \rangle_{L^2(\partial\Omega)} = \delta(m-m')\delta(n-n'), \tag{4.11}$$

$$\langle \nu \times \big(b_n \boldsymbol{v}^{\dagger}_{1,m,n} + \boldsymbol{u}^{\dagger}_{1,m,n}\big),\ \boldsymbol{u}^{\dagger}_{2,m',n'} + d_{3,n'} \boldsymbol{u}^{\dagger}_{3,m',n'} \rangle_{L^2(\partial\Omega)} = \delta(m-m')\delta(n-n'). \tag{4.12}$$

Their explicit values can be computed by

$$\overline{d_{4,n}} = -\frac{1 + a_n c^{jh}_n + c_{n,1,2}}{a_n c^{jh}_{n,2,4} + c_{n,2,4}}, \quad \overline{d_{3,n}} = \frac{1 - (b_n \overline{c^{hj}_{n,1,2}} + \overline{c_{n,1,2}})}{b_n c^{jh}_{n,1,3} + c_{n,1,3}}, \tag{4.13}$$

where c_{n,τ_1,τ_2} are defined in (A.10), and

$$d^{jh}_n = \frac{(n+1) j_n(k) - k j_{n+1}(k)}{k} \overline{h^{(1)}_n(k)}, \quad c^{hj}_n = \frac{(n+1) h^{(1)}_n(k) - k h^{(1)}_{n+1}(k)}{k} \overline{j^{(1)}_n(k)}, \quad c^{jh}_{n,1,3} = \frac{j_n(k) \overline{h^{(1)}_n(k)}}{k} \sqrt{n^2+n}.$$

Similarly to the derivations of (3.20)-(3.21), we can derive a family of probing functions that can induce kernel functions appeared in equations (3.18) and (3.19) with respect to Ψ_x:

$$\tilde{\boldsymbol{w}}^{1,\gamma}_z(y) = \sum_{m,n} (n^2+n)^{\gamma} \Big[\boldsymbol{v}_{2,m,n}(z)\big(\boldsymbol{u}^{\dagger}_{1,m,n}(y) + d_{4,n} \boldsymbol{u}^{\dagger}_{4,m,n}(y)\big) + \boldsymbol{v}_{1,m,n}(z)\big(\boldsymbol{u}^{\dagger}_{2,m,n}(y) + d_{3,n} \boldsymbol{u}^{\dagger}_{3,m,n}(y)\big)\Big], \tag{4.14}$$

$$\tilde{\boldsymbol{w}}^{2,\gamma}_z(y) = \sum_{m,n} (n^2+n)^{\gamma} \Big[\boldsymbol{v}_{1,m,n}(z)\big(\boldsymbol{u}^{\dagger}_{1,m,n}(y) + d_{4,n} \boldsymbol{u}^{\dagger}_{4,m,n}(y)\big) + \boldsymbol{v}^{\dagger}_{2,m,n}(z)\big(\boldsymbol{u}^{\dagger}_{2,m,n}(y) + d_{3,n} \boldsymbol{u}^{\dagger}_{3,m,n}(y)\big)\Big]. \tag{4.15}$$

The numerator of corresponding kernel functions as defined in (2.15) for $\tilde{\boldsymbol{w}}^{i,\gamma}_z$ $(i = 1, 2)$ will then be

$$\langle \nu \times (\Psi_x \cdot \boldsymbol{c}_x),\ \tilde{\boldsymbol{w}}^{1,\gamma}_z \cdot \boldsymbol{p}_z \rangle_{L^2(\partial\Omega)} = \langle \nu \times (\nabla_x \times \Psi_x \cdot \boldsymbol{c}_x),\ \tilde{\boldsymbol{w}}^{2,\gamma}_z \cdot \boldsymbol{q}_z \rangle_{L^2(\partial\Omega)} = \boldsymbol{c}^T_x\, \Xi^{\gamma}_1(x,z) \overline{\boldsymbol{p}_z}, \tag{4.16}$$

$$\langle \nu \times (\Psi_x \cdot \boldsymbol{c}_x),\ \tilde{\boldsymbol{w}}^{2,\gamma}_z \cdot \boldsymbol{p}_z \rangle_{L^2(\partial\Omega)} = \langle \nu \times (\nabla_x \times \Psi_x \cdot \boldsymbol{c}_x),\ \tilde{\boldsymbol{w}}^{1,\gamma}_z \cdot \boldsymbol{p}_z \rangle_{L^2(\partial\Omega)} = \boldsymbol{d}^T_x\, \Xi^{\gamma}_2(x,z) \overline{\boldsymbol{p}_z}, \tag{4.17}$$

where Ξ^{γ}_1 and Ξ^{γ}_2 are the same as in (3.18).

Therefore, since the kernel functions are the same, the verification of the mutually almost orthogonality property for the current case is identical with our previous verification in section 3. In summary, we are ready to introduce the index functions for the inverse problem (4.1):

$$\tilde{I}^{\gamma}_{mo}(z) := \frac{\langle \nu \times E_s,\ \tilde{\boldsymbol{w}}^{1,\gamma}_z \cdot \boldsymbol{p}_z \rangle_{L^2(\partial\Omega)}}{n^{\gamma}(z)}, \quad \tilde{I}^{\gamma}_{di}(z) := \frac{\langle \nu \times E_s,\ \tilde{\boldsymbol{w}}^{2,\gamma}_z \cdot \boldsymbol{q}_z \rangle_{L^2(\partial\Omega)}}{n^{\gamma}(z)} \tag{4.18}$$

for recovering Ω_ϵ and Ω_μ separately, where $n^{\gamma}(z) = \big|\sum \mathrm{diat}\{\Xi^{\gamma}_1(z,z)\}\big|^{\frac{1}{2}}$.

Similar to our discussions in section 3.3, we can derive a family of probing functions that improves the accuracy of reconstruction in the radial direction and the corresponding index functions.

We end this section with an important remark about the choice of probing directions that are needed in (4.18). Unlike in the previous section, we do not know the incident field now. To do so, we first notice that the inner product between the measurement data and probing functions can be written as

$$\langle \nu \times E_s,\ \tilde{\boldsymbol{w}}^{1,\gamma}_z \cdot \boldsymbol{p}_z \rangle_{L^2(\partial\Omega)} = \int_{\partial\Omega} (\nu \times E_s) \cdot \overline{\tilde{\boldsymbol{w}}^{1,\gamma}_z \cdot \boldsymbol{p}_z} dy = \int_{\partial\Omega} \overline{\tilde{\boldsymbol{w}}^{1,\gamma}_z} \cdot (\nu \times E_s) dy\, \overline{\boldsymbol{p}_z}. \tag{4.19}$$

Hence, by taking $\boldsymbol{p}_z = \frac{\int_{\partial\Omega} \overline{\tilde{\boldsymbol{w}}^{1,\gamma}_z} \cdot (\nu \times E_s) dy}{||\int_{\partial\Omega} \overline{\tilde{\boldsymbol{w}}^{1,\gamma}_z} \cdot (\nu \times E_s) dy||_2}$ and $\boldsymbol{q}_z = \frac{\int_{\partial\Omega} \overline{\tilde{\boldsymbol{w}}^{2,\gamma}_z} \cdot (\nu \times E_s) dy}{||\int_{\partial\Omega} \overline{\tilde{\boldsymbol{w}}^{2,\gamma}_z} \cdot (\nu \times E_s) dy||_2}$, then

$$\tilde{I}^{\gamma}_{mo}(z) = \frac{1}{n^{\gamma}(z)} \frac{|\int_{\partial\Omega} \overline{\tilde{\boldsymbol{w}}^{1,\gamma}_z} \cdot (\nu \times E_s) dy|^2}{||\int_{\partial\Omega} \overline{\tilde{\boldsymbol{w}}^{1,\gamma}_z} \cdot (\nu \times E_s) dy||_2}, \quad \tilde{I}^{\gamma}_{di}(z) = \frac{1}{n^{\gamma}(z)} \frac{|\int_{\partial\Omega} \overline{\tilde{\boldsymbol{w}}^{2,\gamma}_z} \cdot (\nu \times E_s) dy|^2}{||\int_{\partial\Omega} \overline{\tilde{\boldsymbol{w}}^{2,\gamma}_z} \cdot (\nu \times E_s) dy||_2}. \tag{4.20}$$

For each sampling point z, the above choices of probing directions ensure that we maximize the magnitude of the absolute value of index functions in all possible choices of $\boldsymbol{p}_z$, $\boldsymbol{q}_z$ and allow us to preserve all possible maximum points of index functions.

Moreover, the above choices of $\boldsymbol{p}_z$ and $\boldsymbol{q}_z$ are also approximations to $E(z)$ and $\nabla \times E(z)$ as in the previous section. For instance, considering $\boldsymbol{p}_z$, recalling the expansion of boundary measurement in (4.6), then the numerator of the above choice of $\boldsymbol{p}_z$ equals to

$$\begin{aligned}\int_{\partial\Omega} \overline{\tilde{\boldsymbol{w}}_z^{1,\gamma}} \cdot (\nu \times E_s) dy &\approx \sum_i a_i \langle \nu \times (\Psi_{x_i} \cdot E(x_i)),\ \tilde{\boldsymbol{w}}_z^{1,\gamma} \cdot \boldsymbol{p}_z \rangle_{L^2(\partial\Omega)} + \sum_j b_j \langle \nu \times (\nabla \times \Psi_{y_j} \cdot \nabla \times E(x_j)),\ \tilde{\boldsymbol{w}}_z^{1,\gamma} \rangle_{L^2(\partial\Omega)} \\ &\approx \sum_i a_i E(x_i)^T \Xi_1^\gamma(x_i, z) + \sum_j b_j (\nabla \times E(x_j))^T \Xi_2^\gamma(y_j, z)\,. \end{aligned} \tag{4.21}$$

We have verified in section 3 that the magnitude of $\Xi_1^\gamma(x_i, z)$ and $\Xi_2^\gamma(y_j, z)$ are small for x_i, y_j not close to z, therefore we see $\sum_i a_i E(x_i)^T \Xi_1^\gamma(x_i, x_n) + \sum_j b_j (\nabla \times E(x_j))^T \Xi_2^\gamma(y_j, x_n) \approx a_n \boldsymbol{c}_n^T \Xi_1^\gamma(x_n, x_n)$ for x_n that is associated with an electric monopole. Therefore, our choice of $\boldsymbol{p}_z$ is approximately equal to $E(x_n)\Xi_1(x_n, x_n)$ after normalization. We may further recall from the expressions of kernel functions in (3.15) that the kernel function that we obtained as a matrix valued function is diagonally dominant when $z \approx x$, and with approximately the same positive diagonal entry. In this case, we conclude that $\boldsymbol{p}_{x_n}$, $\Xi_1^\gamma(x_n, x_n)E(x_n)$, and $E(x_n)$ are approximately equal after normalization.

5. Numerical experiments

We will present a series of numerical experiments in $\mathbb{R}^3$ to demonstrate the robustness, accuracy, and efficiency of the novel DSM. The sampling domain Ω is taken to be the unit ball $B(0, 1)$, with the homogeneous background $\epsilon_0 = \mu_0 = 1$. The forward problem is solved using the second-order edge elements with the maximum volume being 2×10^{-3}. To obtain an accurate solution in a bounded simulation domain, a perfectly matched layer is placed in $[-5, 5]^3 \setminus \Omega$. After formulating the corresponding stiffness matrix and the load vector, we employ the software MUMPS [2] to obtain the noise-free measurement data.

The measurement data, i.e., $\nu \times E^s$ for examples 1 to 4, or $\nu \times^s$ and $\nu \times \nabla \times E$ for example 5, are assumed to be available on a set of discrete measurement points $\Gamma_{\mathbb{S}^2}$ that is uniformly distributed on the unit sphere $\mathbb{S}^2$. An additive Gaussian noise is added to the data to illustrate the robustness of the DSM against noise, with the noisy data given by

$$\nu \times \widetilde{E}^s(y_i) = (\nu \times E^s(y_i))(1 + \epsilon\delta)\,, \quad y_i \in \Gamma_{\mathbb{S}^2}\,, \tag{5.1}$$

where $\nu \times E^s(y)$ is the exact data of the scattered field. We add a quite big noise in the data in all the experiments, namely, we will take $\epsilon = 10\%$, and δ to be randomly and uniformly distributed in $[-1, 1]$.

In addition to the index functions defined in (3.22) and (3.59), we will also use two combined index functions, which are defined by the geometric mean of the previous two index functions as follows:

$$I_{mo}(z) = \left| \frac{I_{mo}^\gamma(z)}{\max_{x\in\Omega}|I_{mo}^\gamma(x)|} \cdot \frac{I_{mo}^R(z)}{\max_{x\in\Omega}|I_{mo}^R(x)|} \right|^{\frac{1}{2}}, \quad I_{di}(z) = \left| \frac{I_{di}^\gamma(z)}{\max_{x\in\Omega}|I_{di}^\gamma(x)|} \cdot \frac{I_{di}^R(z)}{\max_{x\in\Omega}|I_{di}^R(x)|} \right|^{\frac{1}{2}}. \tag{5.2}$$

An intuitive motivation for using the geometric mean for a combined index function is the index can be regarded as a likelihood that represents the likelihood of a sampling point lying in Ω_ϵ or Ω_μ. Hence, the method is expected to identify a region that has a large likelihood to be the support of inhomogeneous inclusions with very limited data, e.g., the data from a single or two incident fields with the same frequency. Therefore, the product index function is approximately a joint likelihood if we assume the likelihood along the angular and radial directions are almost independent.

We remark that we will choose $\gamma = 1$ or 0 for all our numerical experiments. The first reason is that the improvement of the reconstruction accuracy is mild with $\gamma > 1$, based on our numerical observations in section 3.2.2. The second reason is that as γ becomes larger, the proposed index functions are usually more sensitive to inhomogeneous inclusions that are close to the measurement surface. To see that, we can observe from (3.45) that there is a term associated with r_x which makes the magnitude of $K^{1,1}_{\boldsymbol{c}_x,\boldsymbol{p}_x}(x, x)$ larger as x gets closer to $\partial\Omega$. This sensitivity is also confirmed by our numerical experiences. Hence, we suggest choosing $\gamma = 1$ in practice to ensure reasonable reconstructions, especially in the case of multiple inhomogeneous inclusions.

In our numerical experiments, we first carry out an offline computation, namely, to compute the probing functions defined in (3.20), (3.46), and (4.14) with $0 \le n \le 15$ for the summation of spherical vector waves and $z \in \Gamma_\Omega$, where Γ_Ω is a set of points that are approximately uniformly distributed in Ω with the distance between two points smaller than 0.1. Then we compute the index functions defined in (3.22), (3.59), and (5.2) accordingly to recover the support of inhomogeneous inclusions.

In the figures below, the leftmost plot is the distribution of the true inhomogeneous inclusions, where the yellow color represents inhomogeneous inclusions associated with ϵ while the blue color represents inhomogeneous inclusions associated with μ. The second plot is the reconstruction of Ω_ϵ, marked in yellow, by I_{mo}^1, I_{mo}^R, or their combined index. The

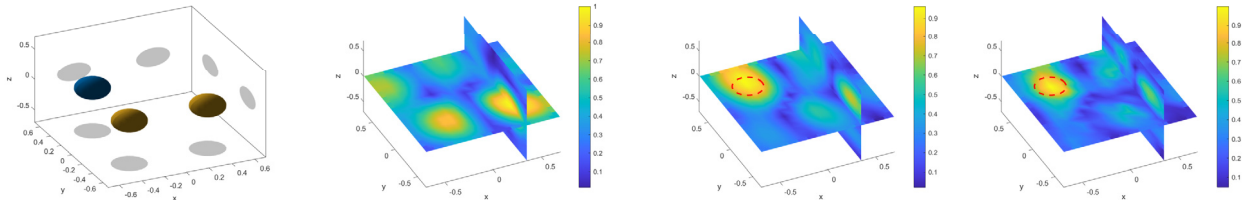

Fig. 4. Example 1. Two inhomogeneous inclusions associated with $\epsilon = 1.3$ are located at balls $B(x_1, 0.15)$ and $B(x_2, 0.15)$, with $x_1 = (0.35, -0.35, 0)$ and $x_2 = (-0.35, -0.35, 0)$; one inhomogeneous inclusion associated with $\mu = 0.55$ is located at the ball $B(x_3, 0.15)$, with $x_3 = (-0.35, 0.35, 0)$. Only one single measurement data is available with $E^i(x) = \boldsymbol{p}e^{i6x\cdot\boldsymbol{d}}$ for $\boldsymbol{p} = (0, 1, 1)/\sqrt{2}$, $\boldsymbol{d} = (0, -1, 1)/\sqrt{2}$. From left to right: true inhomogeneous inclusions, recovered ones by $I^1_{mo}(z)$, $I^1_{di}(z)$, and $I_{di}(z)$.

remaining plots are the reconstruction of Ω_μ, marked in blue, by I^1_{di}, I^R_{di}, or their combination. For all index functions, we always plot the normalized absolute value by their maximum values so that the maximum value of each index function is 1 in the entire sampling domain Ω. For each index function, two cross-sections are plotted, which are chosen to be two of $S_1 = [-\sqrt{2}, \sqrt{2}] \times [-\sqrt{2}, \sqrt{2}] \times 0$, $S_2 = -0.35 \times [-\sqrt{2}, \sqrt{2}] \times [-\sqrt{2}, \sqrt{2}]$, and $S_3 = 0.35 \times [-\sqrt{2}, \sqrt{2}] \times [-\sqrt{2}, \sqrt{2}]$.

Example 1. This example first examines the accuracy and robustness of the index functions $I^1_{mo}(z)$ and $I^1_{di}(z)$ defined in (3.22) with $\gamma = 1$ for recovering the support of inhomogeneous inclusions with different physical nature, and then compare the accuracy of the reconstruction by $I^1_{di}(z)$ and the combined index function defined in (5.2); see Fig. 4. The first two inhomogeneous inclusions associated with $\epsilon = 1.3$ are located within two balls $B(x_1, 0.15)$ and $B(x_2, 0.15)$, with $x_1 = (0.35, -0.35, 0)$ and $x_2 = (-0.35, -0.35, 0)$. And an inhomogeneous inclusion associated with $\mu = 0.55$ is located within the ball $B(x_3, 0.15)$, with $x_3 = (-0.35, 0.35, 0)$. Only one single set of boundary measurement data is available which is induced by the incident field $\boldsymbol{p}e^{i6x\cdot\boldsymbol{d}}$ with $\boldsymbol{p} = (0, 1, 1)/\sqrt{2}$ and $\boldsymbol{d} = (0, -1, 1)/\sqrt{2}$.

Comparing the second and third plots in Fig. 4, the index functions I^1_{mo} and I^1_{di} can both identify the physical properties of inhomogeneous inclusions of two different nature and recover their locations, with only one single set of boundary measurement data. Moreover, we observe from the third plot that the reconstruction of the inhomogeneous inclusion associated with μ, whose real boundary is marked in black, is less accurate, i.e., the size of the reconstructed inhomogeneous inclusions by I^1_{di} is clearly larger than the real one. However, the combined index function can provide a much more accurate reconstruction of Ω_μ (see the fourth plot). Therefore, we will use the combined index function defined in (5.2) in the following examples.

Example 2. This example compares the reconstruction performance with two different wave numbers. Two inhomogeneous inclusions are present, with the first one associated with $\epsilon = 2.2$, being a rectangular bar located at $[0.3, 0.4] \times [-0.4, 0.4] \times [-0.05, 0.05]$, and the second one associated with $\mu = 0.8$ located within the ball $B(x_1, 0.15)$, with $x_1 = (-0.35, 0.35, 0)$; see Fig. 5 where the boundaries of true inhomogeneous inclusions are marked in black. Only the measurement data from a single incident field is used, i.e., from $\boldsymbol{p}e^{ikx\cdot\boldsymbol{d}}$ for $\boldsymbol{p} = (1, 1, -1)/\sqrt{3}$ and $\boldsymbol{d} = -(1, 1, 2)/\sqrt{6}$. The combined index functions (5.2) are employed for reconstructions.

We can observe from Fig. 5 that the location of ϵ and μ are recovered for both $k = 4$ and $k = 8$, with the data from only a single incident field. The shapes of two inhomogeneous inclusions, especially the rectangular bar associated with ϵ, are recovered clearly more accurately with the incident field from the larger frequency (i.e., $k = 8$).

Example 3. This example examines the reconstructions of anisotropic inhomogeneous inclusions by the combined index functions (5.2). We consider the following ϵ_1 and ϵ_2:

$$\epsilon_1 = \begin{pmatrix} 3 & 0.3 & 0.4 \\ 0.3 & 2.8 & 0.2 \\ 0.4 & 0.2 & 1.8 \end{pmatrix}, \quad \epsilon_2 = \begin{pmatrix} 2.5 & 0.3 & 0.4 \\ 0.3 & 3 & 0.2 \\ 0.4 & 0.2 & 2 \end{pmatrix}, \tag{5.3}$$

with the corresponding inhomogeneous inclusions being located at balls $B(x_1, 0.15)$ and $B(x_2, 0.15)$, with $x_1 = (0.4, 0.1, 0)$ and $x_2 = (-0.4, -0.1, 0)$. For μ_1 and μ_2, we consider the following matrices:

$$\mu_1 = \begin{pmatrix} 1/3 & 10 & 4 \\ 10 & 1/6 & 5 \\ 4 & 5 & 1/6 \end{pmatrix}, \quad \mu_2 = \begin{pmatrix} 0.2 & 5 & 8 \\ 5 & 0.2 & 4 \\ 8 & 4 & 0.2 \end{pmatrix}, \tag{5.4}$$

with the corresponding inhomogeneous inclusions being located at balls $B(x_3, 0.15)$ and $B(x_4, 0.15)$, with $x_3 = (-0.1, 0.4, 0)$ and $x_4 = (0.1, -0.4, 0)$. Only the boundary data from a single incident field is used, i.e., $\boldsymbol{p}e^{i8x\cdot\boldsymbol{d}}$ for $\boldsymbol{p} = (-1, 1, 1)/\sqrt{3}$ and $\boldsymbol{d} = -(2, 1, 1)/\sqrt{6}$.

This is a quite difficult example: the inhomogeneous inclusions are associated with two fully anisotropic parameters ϵ and μ; four inhomogeneous inclusions are close to each other; many components of ϵ and μ differ significantly (the

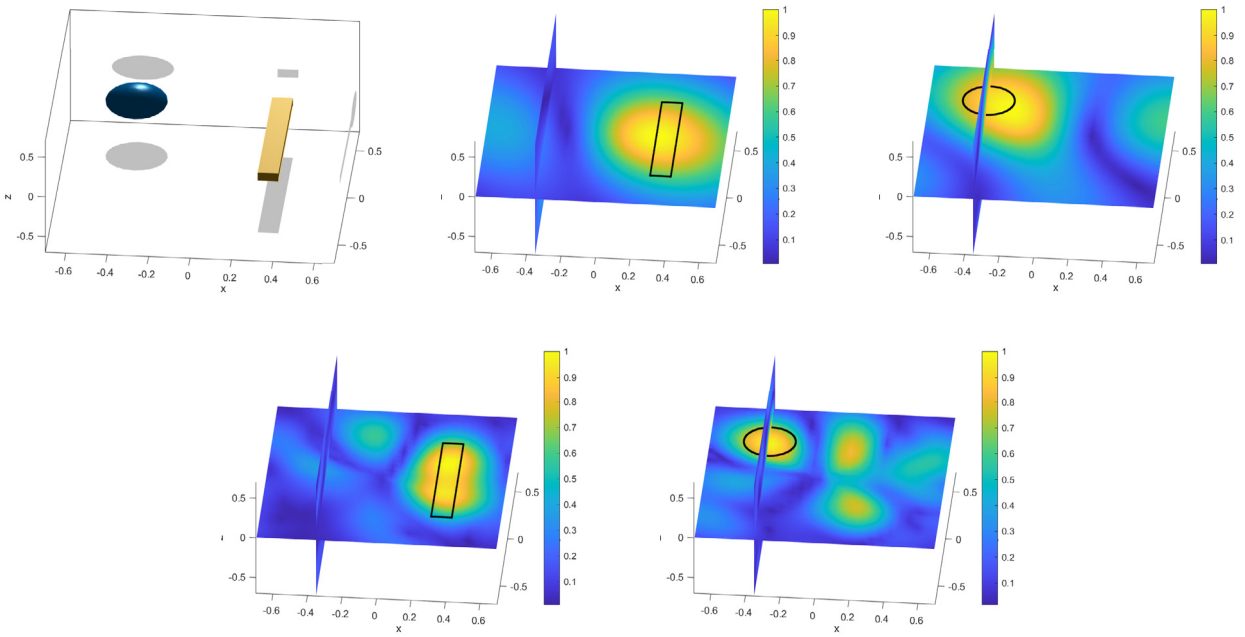

Fig. 5. Example 2. The first inhomogeneous inclusion associated with $\mu = 0.8$ is located at the ball $B(x_1, 0.15)$, with $x_1 = (-0.35, 0.35, 0)$; the second inhomogeneous inclusion associated with $\epsilon = 2.2$ is located at $[0.3, 0.4] \times [-0.4, 0.4] \times [-0.05, 0.05]$. The data used is from the single incident $E^i(x) = \boldsymbol{p}e^{ikx\cdot\boldsymbol{d}}$, with $\boldsymbol{p} = (1, 1, -1)/\sqrt{3}$, $\boldsymbol{d} = -(1, 1, 2)/\sqrt{6}$. First row from left to right: true inhomogeneous inclusions, recovered ones by I_{mo} and I_{di} with $k = 4$; second row from left to right: recovered ones by I_{mo} and I_{di} with $k = 8$.

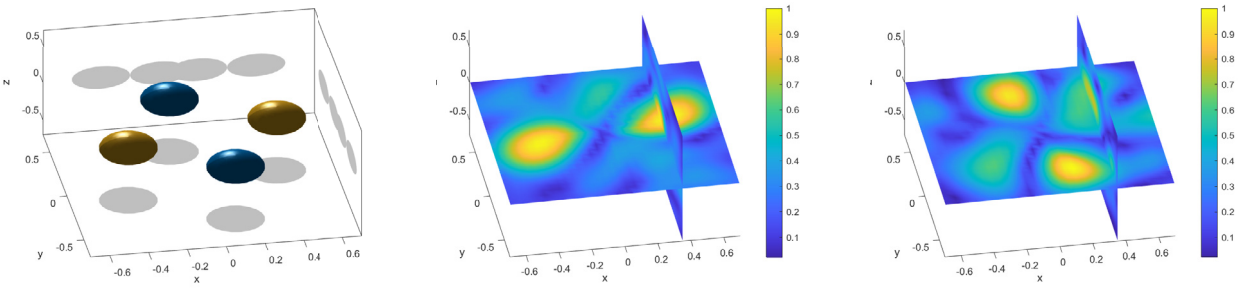

Fig. 6. Example 3. Two inhomogeneous inclusions associated with ϵ_1 and ϵ_2 defined in (5.4) are located at balls $B(x_1, 0.15)$ and $B(x_2, 0.15)$, with $x_1 = (0.4, 0.1, 0)$ and $x_2 = (-0.4, -0.1, 0)$. Two inhomogeneous inclusions associated with μ_1 and μ_2 defined in (5.3) are located at $B(x_3, 0.15)$ and $B(x_4, 0.15)$ with $x_3 = (-0.1, 0.4, 0)$ and $x_4 = (0.1, -0.4, 0)$. The data is from a single incidence $E^i(x) = \boldsymbol{p}e^{i8x\cdot\boldsymbol{d}}$, with $\boldsymbol{p} = (-1, 1, 1)/\sqrt{3}$ and $\boldsymbol{d} = -(2, 1, 1)/\sqrt{6}$. From left to right: true inhomogeneous inclusions, recovered ones by I_{mo}, and I_{di}.

maximum ratio between ϵ and μ in the diagonals is as high as 16.8, while the ratios between the off-diagonal entries are as high as 30). But we can observe from Fig. 6 that the numerical reconstructions are still quite satisfactory to recover the locations, shapes, and sizes of all inhomogeneous inclusions, in view of the measurement data from only one single incident field.

Example 4. This example examines a very challenging case where one type of inhomogeneous inclusions is totally embedded in the other type. An inhomogeneous inclusion associated with $\mu = 0.4$ is located at $B(x_1, 0.1)$ with $x_1 = (-0.2, 0, 0)$ and fully embedded in another type of inhomogeneous inclusions associated with $\epsilon = 2.5$, which is located in a spherical shell centered at the origin with an inner sphere and an outer sphere of radii being 0.35 and 0.38 respectively. For this challenging example, we combine the index functions I_{mo} and I_{di} that are generated by two sets of boundary measurement data, similarly to what we did in (5.2) by using their geometric mean. The two sets of boundary measurement data are induced by the incident fields $\boldsymbol{p}_1 e^{i8x\cdot\boldsymbol{d}_1}$ and $\boldsymbol{p}_2 e^{i8x\cdot\boldsymbol{d}_2}$, with $\boldsymbol{p}_1 = (1, -1, 1)/\sqrt{3}$, $\boldsymbol{d}_1 = (0, 1, 1)/\sqrt{2}$, $\boldsymbol{p}_2 = (0, -1, 1)/\sqrt{2}$ and $\boldsymbol{d}_2 = (0, -1, -1)/\sqrt{2}$.

We can observe from Fig. 7 that the DSM still works quite effectively for this very challenging reconstruction: the shape of the spherical shell is recovered quite properly by I_{mo} (second plot) while the inhomogeneous inclusion associated with μ, that is completely embedded in the outer shell, can be also recovered from I_{di} (third plot).

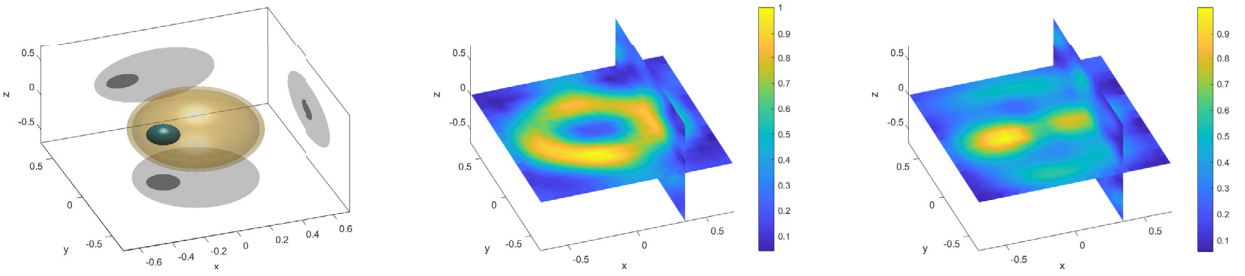

Fig. 7. Example 4. One inhomogeneous inclusions associated with $\mu = 0.4$ is located at the ball $B(x_1, 0.1)$, with $x_1 = (-0.2, 0, 0)$; one inhomogeneous inclusion associated with $\epsilon = 2.5$ is located at the spherical shell centered at the origin with the radii of the inner and outer spheres being 0.35 and 0.38 respectively. Two sets of measurement data are available with $E^i(x) = \boldsymbol{p}_i e^{i8x\cdot\boldsymbol{d}_i}$ with $i = 1, 2$, where $\boldsymbol{p}_1 = (1, -1, 1)/\sqrt{3}$, $\boldsymbol{d}_1 = (0, 1, 1)/\sqrt{2}$ and $\boldsymbol{p}_2 = (0, -1, 1)/\sqrt{2}$, $\boldsymbol{d}_2 = (0, -1, -1)/\sqrt{2}$. From left to right: true inhomogeneous inclusions, recovered ones by I_{mo}, and I_{di}.

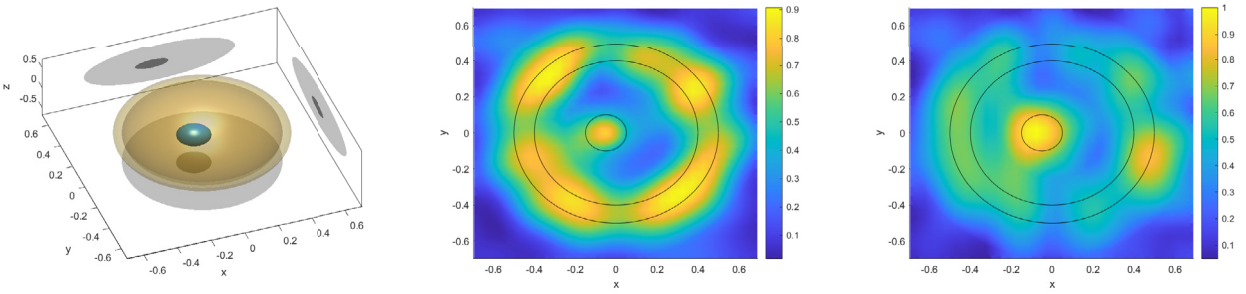

Fig. 8. Example 5. One inhomogeneous inclusion associated with $\epsilon_1 = 2$ is located at the spherical shell centered at the origin with the radii of the inner and outer spheres being 0.45 and 0.5 respectively; the other inhomogeneous inclusions associated with $\epsilon_2 = 1.5$ (middle) and 4 (right) is located at the ball $B(x_1, 0.1)$ with $x_1 = (-0.05, 0, 0)$. The used data is from two incident fields, $\boldsymbol{p}_1 e^{i10x\cdot\boldsymbol{d}_1}$ and $\boldsymbol{p}_2 e^{i10x\cdot\boldsymbol{d}_2}$, with $\boldsymbol{p}_1 = (0, -1, 1)/\sqrt{2}$, $\boldsymbol{d}_1 = (0, 1, 1)/\sqrt{2}$, $\boldsymbol{p}_2 = (1, 1, 0)/\sqrt{2}$ and $\boldsymbol{d}_2 = (-1, 1, 0)/\sqrt{2}$. From left to right: true inhomogeneous inclusions, recovered ones by I_{mo} with $\epsilon_2 = 1.5$ and 4, respectively.

Example 5. In this example, we apply the DSM to the case when there are two inhomogeneous inclusions of the same type (i.e., both from electric permittivities but with different values). The first inhomogeneous inclusion is associated with $\epsilon_1 = 2$ and located in a spherical shell centered at the origin, with the inner sphere and the outer sphere of radii being 0.45 and 0.5 respectively. The second inhomogeneous inclusion is associated with a different ϵ_2 and located at $B(x_1, 0.1)$ with $x_1 = (-0.05, 0, 0)$. The electromagnetic field is induced by two incidences, $\boldsymbol{p}_1 e^{i10x\cdot\boldsymbol{d}_1}$ and $\boldsymbol{p}_2 e^{i10x\cdot\boldsymbol{d}_2}$, with $\boldsymbol{p}_1 = (0, -1, 1)/\sqrt{2}$, $\boldsymbol{d}_1 = (0, 1, 1)/\sqrt{2}$, $\boldsymbol{p}_2 = (1, 1, 0)/\sqrt{2}$ and $\boldsymbol{d}_2 = (-1, 1, 0)/\sqrt{2}$.

The index function I_{mo} is computed twice for $\epsilon_2 = 1.5$ (middle plot) and $\epsilon_2 = 4$ (right plot), and the slice of the index function at $z = 0$ is plotted in Fig. 8, where the boundaries of two true inclusions are marked in black. We can observe from the second plot of Fig. 8 that the DSM can recover inhomogeneous inclusions of the same type quite accurately when one of them is completely embedded by the other. But we can see from the right plot where ϵ_2 is much larger than ϵ_1, only the embedded inclusion associated with the larger ϵ is recovered accurately. This is reasonable, considering the extremely limited observation data used.

Example 6. In this example, we examine the reconstruction by DSM for the case that was discussed in section 4 when the incident field is unknown, with a single set of the measurement data $\nu \times E$ and $\nu \times \nabla \times E$ collected on the boundary and no any prior information of the incident field. The first inhomogeneities inclusion associated with $\epsilon = 1.2$ is located at the ball $B(x_1, 0.1)$, with $x_1 = (-0.15, 0.35, 0)$, while another inhomogeneous inclusion associated with $\mu = 0.85$ is located at the ball $B(x_2, 0.1)$, with $x_2 = (0.15, -0.35, 0)$. The electromagnetic field is induced by $E^i = \boldsymbol{p}_1 \exp^{i8\boldsymbol{d}_1} + \boldsymbol{p}_2 \exp^{i8\boldsymbol{d}_2}$, with $\boldsymbol{p}_1 = (0, 1, 1)/\sqrt{2}$, $\boldsymbol{d}_1 = (0, -1, 1)/\sqrt{2}$, $\boldsymbol{p}_2 = -(1, 1, 1)/\sqrt{3}$ and $\boldsymbol{d}_2 = (-2, 1, 1)/\sqrt{6}$. Two index functions are computed with only one single set of measurement data for both $\nu \times E|_{\partial\Omega}$ and $\nu \times \nabla \times E|_{\partial\Omega}$. The probing directions are chosen based on (4.20).

From the second plot by I_{mo} and the third plot by I_{di} in the reconstructions in Fig. 9, we can observe that the DSM can still identify the locations and physical properties of the inhomogeneous inclusions associated with ϵ and μ, respectively, quite satisfactorily, with only one single set of noisy measurement data.

6. Concluding remarks

We have proposed a novel DSM to recover the support of electromagnetic inhomogeneous inclusions of different physical nature simultaneously with highly limited data, only one or two sets of noisy boundary measurement data. The new

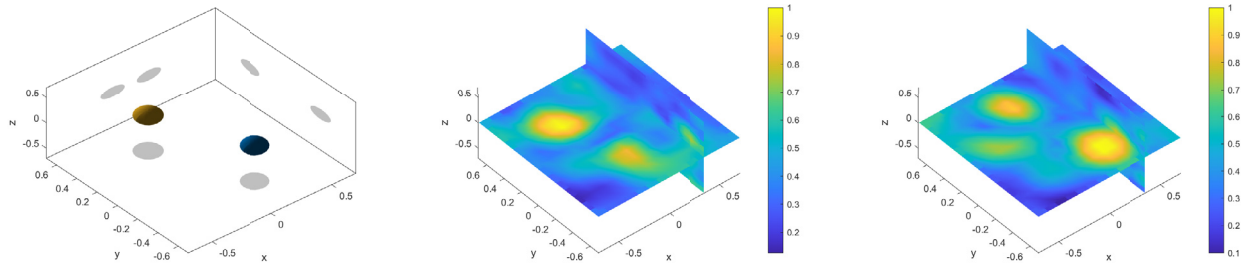

Fig. 9. Example 6. One inhomogeneous inclusions associated with $\epsilon = 1.2$ is located at the ball $B(x_1, 0.1)$, with $x_1 = (-0.15, 0.35, 0)$; one inhomogeneous inclusion associated with $\mu = 0.8$ is located at the ball $B(x_2, 0.1)$, with $x_2 = (0.15, -0.35, 0)$. The electromagnetic field is induced by $E^i = \boldsymbol{p}_1 \exp^{i\mathcal{S}\boldsymbol{d}_1} + \boldsymbol{p}_2 \exp^{i\mathcal{S}\boldsymbol{d}_2}$, with $\boldsymbol{p}_1 = (0, 1, 1)/\sqrt{2}$, $\boldsymbol{d}_1 = (0, -1, 1)/\sqrt{2}$; $\boldsymbol{p}_2 = -(1, 1, 1)/\sqrt{3}$, $\boldsymbol{d}_2 = (-2, 1, 1)/\sqrt{6}$. One single set of boundary measurements for both $\nu \times E$ and $\nu \times \nabla \times E$ is available, with no prior information on the incident field. From left to right: true inhomogeneous inclusions, recovered ones by I_{mo}, and I_{di}.

DSM leverages upon the important mutually almost orthogonality property between fundamental solutions of the forward problem and two proper sets of probing functions.

Two novel families of probing functions are constructed to obtain accurate reconstruction results in the direction that is parallel to and vertical to the measurement surface separately. The design of the first family is based on the observation that applying a surface Laplacian operator on the probing function can improve the accuracy of the reconstruction. For the second family, it is constructed such that the corresponding kernel function approximates a Gaussian kernel in the direction that is vertical to the measurement surface. Therefore, it can recover inhomogeneous inclusions distributed in the radial direction satisfactorily. The desired mutually almost orthogonality property is carefully verified for the two new families of probing functions by both theoretical analysis and numerical demonstration. From our extensive numerical experiments, the method is shown to be completely parallel, easy to implement, fast to compute, and robust under noisy and limited measurement data.

For future research, several topics can be further explored along with the current work. Firstly, it is interesting to extend the proposed DSM to a broader class of coefficients inverse problems with more complicated interaction terms, for instance, fully anisotropic linear and nonlinear elasticity model, shallow water wave equation, Boltzmann transport equation, Klein-Gordon, and Sine-Gordon equations, etc. More generally, it is important to develop a consistent and unified framework of direct sampling type methods for general inverse problems. This framework could provide us concrete guidance on the optimal choice of probing functions, allow a more rigorous justification of the proposed method, and validate the direct sampling type methods in many other inverse problems arising in real applications.

CRediT authorship contribution statement

Yat Tin Chow: Conceptualization, Investigation, Methodology, Writing – review & editing. **Fuqun Han:** Conceptualization, Formal analysis, Investigation, Methodology, Software, Validation, Visualization, Writing – original draft. **Jun Zou:** Conceptualization, Methodology, Project administration, Supervision, Writing – review & editing.

Declaration of competing interest

The authors declare that they have no known competing financial interests or personal relationships that could have appeared to influence the work reported in this paper.

Data availability

Data will be made available on request.

Acknowledgement

The authors are very grateful to two referees for their constructive comments and suggestions, which have led to great improvement in both the results and the presentation of the paper.

Appendix A. Review on spherical vector waves

Some fundamental results related to spherical vector waves that will be used repeatedly throughout our discussion are reviewed in this appendix. The primary motivation for introducing them is that they provide a convenient way to represent differential operators on the unit sphere. In the following, we shall write $x = (r_x, \theta_x, \phi_x)$ in spherical coordinates.

Firstly, denoting spherical harmonics of order (m, n) as

$$Y_n^m(\hat{x}) = \sqrt{\frac{2n+1}{4\pi}\frac{(n-|m|)!}{(n+|m|)!}} P_n^{|m|}(\cos\theta_x) e^{im\phi_x}, \quad -n \le m \le n, \quad n \in \mathbb{N}, \quad m \in \mathbb{Z}, \tag{A.1}$$

where P_n^m is the associated Legendre polynomial. The Laplacian operator on the unit sphere acting on spherical harmonics leads to

$$(-\Delta_{\mathbb{S}^2}) Y_n^m(\hat{x}) = -(n^2+n) Y_n^m(\hat{x}). \tag{A.2}$$

Since the electromagnetic field is a vector field, we need to introduce vector spherical harmonics on $\mathbb{S}^2$ under spherical basis $(\hat{\boldsymbol{r}}, \hat{\boldsymbol{\theta}}, \hat{\boldsymbol{\phi}})$ which are

$$\begin{cases} A_{1,m,n}(\hat{x}) = (n^2+n)^{-\frac{1}{2}} \nabla Y_n^m(\theta, \phi) \times \hat{\boldsymbol{r}} = (n^2+n)^{-\frac{1}{2}} \left(\hat{\boldsymbol{\theta}} \frac{1}{\sin\theta} \frac{\partial Y_n^m(\hat{x})}{\partial \phi} - \hat{\boldsymbol{\phi}} \frac{\partial Y_n^m(\hat{x})}{\partial \theta} \right), \\ A_{2,m,n}(\hat{x}) = (n^2+n)^{-\frac{1}{2}} \nabla Y_n^m(\hat{x}) = (n^2+n)^{-\frac{1}{2}} \left(\hat{\boldsymbol{\theta}} \frac{\partial Y_n^m(\hat{x}}{\partial \theta} + \hat{\boldsymbol{\phi}} \frac{1}{\sin\theta} \frac{\partial Y_n^m(\hat{x})}{\partial \phi} \right), \\ A_{3,m,n}(\hat{x}) = \hat{\boldsymbol{r}} Y_n^m(\hat{x}); \end{cases} \tag{A.3}$$

and $A_{1,0,0} = A_{2,0,0} = 0$. The system of vector spherical harmonics $\{A_{\tau,m,n} | \, \tau = 1, 2, 3, \ -n \le m \le n, \ n \in \mathbb{N}\}$ forms a complete and orthonormal basis for vector fields on the spherical surface.

In our work, we have also used repeatedly the product of two vector spherical harmonics, which are

$$\begin{aligned}
A_{1,m,n}(\hat{x}) A_{1,m,n}^\dagger(\hat{z}) =& \frac{1}{n^2+n} \Big[\frac{1}{\sin\theta_x \sin\theta_z} \frac{\partial Y_n^m(\hat{x})}{\partial \phi_x} \frac{\partial \overline{Y_n^m}(\hat{z})}{\partial \phi_z} \hat{\boldsymbol{\theta}}_x \hat{\boldsymbol{\theta}}_z - \frac{1}{\sin\theta_x} \frac{\partial Y_n^m(\hat{x})}{\partial \phi_x} \frac{\partial \overline{Y_n^m}(\hat{z})}{\partial \theta_z} \hat{\boldsymbol{\theta}}_x \hat{\boldsymbol{\phi}}_z \\
& - \frac{1}{\sin\theta_z} \frac{\partial Y_n^m(\hat{x})}{\partial \theta_x} \frac{\partial \overline{Y_n^m}(\hat{z})}{\partial \phi_z} \hat{\boldsymbol{\phi}}_x \hat{\boldsymbol{\theta}}_z + \frac{\partial Y_n^m(\hat{x})}{\partial \theta_x} \frac{\partial \overline{Y_n^m}(\hat{z})}{\partial \theta_z} \hat{\boldsymbol{\phi}}_x \hat{\boldsymbol{\phi}}_z \Big]; \\
A_{2,m,n}(\hat{x}) A_{2,m,n}^\dagger(\hat{z}) =& \frac{1}{n^2+n} \Big[\frac{\partial Y_n^m(\hat{x})}{\partial \theta_x} \frac{\partial \overline{Y_n^m}(\hat{z})}{\partial \theta_z} \hat{\boldsymbol{\theta}}_x \hat{\boldsymbol{\theta}}_z + \frac{1}{\sin\theta_z} \frac{\partial Y_n^m(\hat{x})}{\partial \theta_x} \frac{\partial \overline{Y_n^m}(\hat{z})}{\partial \phi_z} \hat{\boldsymbol{\theta}}_x \hat{\boldsymbol{\phi}}_z \\
& + \frac{1}{\sin\theta_x} \frac{\partial Y_n^m(\hat{x})}{\partial \phi_x} \frac{\partial \overline{Y_n^m}(\hat{z})}{\partial \theta_z} \hat{\boldsymbol{\phi}}_x \hat{\boldsymbol{\theta}}_z + \frac{1}{\sin\theta_x \sin\theta_z} \frac{\partial Y_n^m(\hat{x})}{\partial \phi_x} \frac{\partial \overline{Y_n^m}(\hat{z})}{\partial \phi_z} \hat{\boldsymbol{\phi}}_x \hat{\boldsymbol{\phi}}_z \Big]; \\
A_{3,m,n}(\hat{x}) A_{3,m,n}^\dagger(\hat{z}) =& Y_n^m(\hat{x}) \overline{Y_n^m}(\hat{x}) \hat{\boldsymbol{r}}_x \hat{\boldsymbol{r}}_z; \\
A_{2,m,n}(\hat{x}) A_{3,m,n}^\dagger(\hat{z}) =& \frac{1}{\sqrt{n^2+n}} \Big[\frac{\partial Y_n^m(\hat{x})}{\partial \theta_x} \overline{Y_n^m}(\hat{z}) \hat{\boldsymbol{\theta}}_x \hat{\boldsymbol{r}}_z + \frac{1}{\sin\theta_x} \frac{\partial Y_n^m(\hat{x})}{\partial \phi_x} \overline{Y_n^m}(\hat{z}) \hat{\boldsymbol{\phi}}_x \boldsymbol{r}_z \Big] \\
A_{1,m,n}(\hat{x}) A_{2,m,n}^\dagger(\hat{z}) =& \frac{1}{n^2+n} \Big[\frac{\partial Y_n^m(\hat{x})}{\sin\theta_x \partial \phi_x} \frac{\partial \overline{Y_n^m}(\hat{z})}{\partial \theta_z} \hat{\boldsymbol{\theta}}_x \hat{\boldsymbol{\theta}}_z + \frac{1}{\sin\theta_x \sin\theta_z} \frac{\partial Y_n^m(\hat{x})}{\partial \phi_x} \frac{\partial \overline{Y_n^m}(\hat{z})}{\partial \phi_z} \hat{\boldsymbol{\theta}}_x \hat{\boldsymbol{\phi}}_z \\
& - \frac{\partial Y_n^m(\hat{x})}{\partial \theta_x} \frac{\partial \overline{Y_n^m}(\hat{z})}{\partial \theta_z} \hat{\boldsymbol{\phi}}_x \hat{\boldsymbol{\theta}}_z - \frac{\partial Y_n^m(\hat{x})}{\partial \theta_x} \frac{\partial \overline{Y_n^m}(\hat{z})}{\sin\theta_z \partial \phi_z} \hat{\boldsymbol{\phi}}_x \hat{\boldsymbol{\phi}}_z \Big], \\
A_{2,m,n}(\hat{x}) A_{1,m,n}^\dagger(\hat{z}) =& \frac{1}{n^2+n} \Big[\frac{\partial Y_n^m(\hat{x})}{\partial \theta_x} \frac{\partial \overline{Y_n^m}(\hat{z})}{\sin\theta_z \partial \phi_z} \hat{\boldsymbol{\theta}}_x \hat{\boldsymbol{\theta}}_z - \frac{\partial Y_n^m(\hat{x})}{\partial \theta_x} \frac{\partial \overline{Y_n^m}(\hat{z})}{\partial \theta_z} \hat{\boldsymbol{\theta}}_x \hat{\boldsymbol{\phi}}_z \\
& + \frac{1}{\sin\theta_x \sin\theta_z} \frac{\partial Y_n^m(\hat{x})}{\partial \phi_x} \frac{\partial \overline{Y_n^m}(\hat{z})}{\partial \phi_z} \hat{\boldsymbol{\phi}}_x \hat{\boldsymbol{\theta}}_z - \frac{\partial Y_n^m(\hat{x})}{\sin\theta_x \partial \phi_x} \frac{\partial \overline{Y_n^m}(\hat{z})}{\partial \theta_z} \hat{\boldsymbol{\phi}}_x \hat{\boldsymbol{\phi}}_z \Big], \\
A_{1,m,n}(\hat{x}) A_{3,m,n}^\dagger(\hat{z}) =& \frac{1}{\sqrt{n^2+n}} \Big[\frac{\partial Y_n^m(\hat{x})}{\sin\theta_x \partial \phi_x} \overline{Y_n^m}(\hat{z}) \hat{\boldsymbol{\theta}}_x \hat{\boldsymbol{r}}_z - \frac{\partial Y_n^m(\hat{x})}{\partial \theta_x} \overline{Y_n^m}(\hat{z}) \hat{\boldsymbol{\phi}}_x \hat{\boldsymbol{r}}_z \Big].
\end{aligned} \tag{A.4}$$

Next, to include the dependence in the radial direction, for $x \in \mathbb{R}^3$, we further define the following spherical vector waves with $k > 0$ as

$$\begin{cases} \boldsymbol{u}_{1,m,n}(x) = h_n^{(1)}(kr_x) A_{1,m,n}(\hat{x}), \\ \boldsymbol{u}_{2,m,n}(x) = \frac{(kr_x h_n^{(1)}(kr_x))'}{kr_x} A_{2,m,n}(\hat{x}) + (n^2+n)^{\frac{1}{2}} \frac{h_n^{(1)}(kr_x)}{kr_x} A_{3,m,n}(\hat{x}), \\ \boldsymbol{u}_{3,m,n}(x) = \frac{1}{k} \nabla (h_n^{(1)}(kr_x) Y_n^m(\hat{x}) = (h_n^{(1)})'(kr_x) A_{3,m,n}(\hat{x}) + (n^2+n)^{\frac{1}{2}} \frac{h_n^{(1)}(kr_x)}{kr_x} A_{2,m,n}(\hat{x}), \end{cases} \tag{A.5}$$

where $h_n^{(1)}$ is the spherical Bessel function of the third kind. The first two types of spherical vector waves are divergence free which can be employed to represent an electromagnetic field. Moreover, they can be considered as electric fields induced by electric multipoles or magnetic multipoles separately that satisfy

$$\nabla \times \boldsymbol{u}_{1,m,n}(x) = k\boldsymbol{u}_{2,m,n}(x)\,, \quad \nabla \times \boldsymbol{u}_{2,m,n}(x) = k\boldsymbol{u}_{1,m,n}(x)\,.$$

Furthermore, the third type of spherical vector waves is curl free, i.e., $\nabla \times \boldsymbol{u}_{3,m,n} = 0$, which completes the system of spherical vector waves for any vector field on the spherical surface [5]. The family of $\boldsymbol{u}_{\tau,m,n}$ is also called radiating spherical vector waves due to the choice of $h_n^{(1)}$ in the radial direction. For the notational sake, we also write

$$\boldsymbol{u}_{4,m,n}(x) := \boldsymbol{u}_{3,m,n} \times \hat{\boldsymbol{r}} = (n^2+n)^{\frac{1}{2}} \frac{h_n^{(1)}(kr)}{kr} A_{1,m,n}(\hat{x})\,. \tag{A.6}$$

At the same time, if the vector field under investigation is regular inside Ω, we have to employ regular spherical vector waves which are defined as

$$\begin{cases} \boldsymbol{v}_{1,m,n}(x) = j_n(kr_x) A_{1,m,n}(\hat{x})\,, \\ \boldsymbol{v}_{2,m,n}(x) = \frac{(kr_x j_n(kr_x))'}{kr_x} A_{2,m,n}(\hat{x}) + (n^2+n)^{\frac{1}{2}} \frac{j_n(kr_x)}{kr_x} A_{3,m,n}(\hat{x})\,, \end{cases} \tag{A.7}$$

where j_n is the spherical Bessel functions of the first kind.

The spherical Laplacian applied on spherical vector waves lead to

$$\begin{cases} (-\Delta)_{\mathbb{S}^2} \boldsymbol{u}_{1,m,n}(x) &= -(n^2+n)\boldsymbol{u}_{1,m,n}(x)\,, \\ (-\Delta)_{\mathbb{S}^2} \boldsymbol{u}_{2,m,n}(x) &= -(n^2+n)\boldsymbol{u}_{2,m,n}(x) + 2(n^2+n)^{\frac{1}{2}} \boldsymbol{v}_{3,m,n}(x)\,, \\ (-\Delta)_{\mathbb{S}^2} \boldsymbol{u}_{3,m,n}(x) &= -(n^2+n+2)\boldsymbol{u}_{3,m,n}(x) + 2(n^2+n)^{\frac{1}{2}} \boldsymbol{u}_{2,m,n}(x)\,, \\ (-\Delta)_{\mathbb{S}^2} \boldsymbol{u}_{4,m,n}(x) &= -(n^2+n)\boldsymbol{u}_{4,m,n}(x)\,. \end{cases} \tag{A.8}$$

As the measurement of the electromagnetic field is usually the tangential field on the boundary, we also need to compute the tangential field of vector spherical harmonics and radiating spherical vector waves, which are

$$\begin{cases} \hat{\boldsymbol{r}} \times A_{1,m,n}(\hat{x}) = A_{2,m,n}(\hat{x})\,, \\ \hat{\boldsymbol{r}} \times A_{2,m,n}(\hat{x}) = -A_{1,m,n}(\hat{x})\,, \\ \hat{\boldsymbol{r}} \times A_{3,m,n}(\hat{x}) = 0\,; \end{cases} \quad \Rightarrow \quad \begin{cases} \hat{\boldsymbol{r}} \times \boldsymbol{u}_{1,m,n}(x) = & h_n^{(1)}(kr_x) A_{2,m,n}(\hat{x})\,, \\ \hat{\boldsymbol{r}} \times \boldsymbol{u}_{2,m,n}(x) = & -\frac{(kr_x h_n^{(1)}(kr_x))'}{kr_x} A_{1,m,n}(\hat{x})\,, \\ \hat{\boldsymbol{r}} \times \boldsymbol{u}_{3,m,n}(x) = & -(n^2+n)^{\frac{1}{2}} \frac{h_n^{(1)}(kr)}{kr} A_{1,m,n}(\hat{x})\,, \\ \hat{\boldsymbol{r}} \times \boldsymbol{u}_{4,m,n}(x) = & (n^2+n)^{\frac{1}{2}} \frac{h_n^{(1)}(kr)}{kr} A_{2,m,n}(\hat{x})\,. \end{cases} \tag{A.9}$$

We now list some orthogonality relationship between spherical vector waves of different types under L^2 inner product on $\mathbb{S}^2$:

$$\begin{aligned} \langle \nu \times \boldsymbol{u}_{1,m,n},\, \boldsymbol{u}_{\tau,m',n'} \rangle_{L^2(\mathbb{S}^2)} &= \delta(m-m')\delta(n-n') c_{n,1,\tau}\,, \quad \text{where } \tau = 2,3\,, \\ \langle \nu \times \boldsymbol{u}_{2,m,n},\, \boldsymbol{u}_{\tau,m',n'} \rangle_{L^2(\mathbb{S}^2)} &= \delta(m-m')\delta(n-n') c_{n,2,\tau}\,, \quad \text{where } \tau = 1,4\,; \end{aligned} \tag{A.10}$$

where those constants are defined as

$$c_{n,1,2} = \frac{\overline{(krh_n^{(1)}(kr))'|_{r=1}}}{k} h_n^{(1)}(k)\,, \quad c_{n,1,3} = \frac{|h_n^{(1)}(k)|^2}{k}\,, \quad c_{n,2,4} = c_{n,1,2}\frac{(n^2+n)^{\frac{1}{2}}}{k}\,, \quad c_{n,2,1} = \overline{c_{n,1,2}}\,.$$

At the same time, the remaining possible inner product between radiating spherical vector waves are all zero, i.e.,

$$\begin{aligned} &\langle \nu \times \boldsymbol{u}_{1,m,n},\, \boldsymbol{u}_{4,m',n'} \rangle_{L^2(\mathbb{S}^2)} = 0\,, \quad \langle \nu \times \boldsymbol{u}_{2,m,n},\, \boldsymbol{u}_{3,m',n'} \rangle_{L^2(\mathbb{S}^2)} = 0\,; \\ &\langle \nu \times \boldsymbol{u}_{1,m,n},\, \boldsymbol{u}_{1,m',n'} \rangle_{L^2(\mathbb{S}^2)} = 0\,, \quad \langle \nu \times \boldsymbol{u}_{2,m,n},\, \boldsymbol{u}_{2,m',n'} \rangle_{L^2(\mathbb{S}^2)} = 0\,. \end{aligned}$$

We notice that, due to the definition of $\boldsymbol{u}^{\dagger}_{\tau,m,n}$ does not take the complex conjugate on $h_n^{(1)}$, all the above relationships hold after replacing all $\boldsymbol{u}_{\tau,m,n}$ by $\boldsymbol{u}^{\dagger}_{\tau,m,n}$.

We would like to remark that all the above relationships hold for the case using regular spherical vector waves $\boldsymbol{v}_{\tau,m,n}$ after replacing $h_n^{(1)}(kr)$ by $j_n(kr)$.

References

[1] M. Afsar, A. Sharma, M. Obol, Microwave permittivity and permeability properties and microwave reflections of micro/nano ferrite powders, in: 2009 IEEE Instrumentation and Measurement Technology Conference, IEEE, 2009, pp. 274–278.

[2] P. Amestoy, I.S. Duff, J. Koster, J.-Y. L'Excellent, A fully asynchronous multifrontal solver using distributed dynamic scheduling, SIAM J. Matrix Anal. Appl. 23 (2001) 15–41.

[3] H. Ammari, E. Iakovleva, D. Lesselier, G. Perrusson, Music-type electromagnetic imaging of a collection of small three-dimensional inclusions, SIAM J. Sci. Comput. 29 (2007) 674–709.

[4] H. Ammari, A. Khelifi, Electromagnetic scattering by small dielectric inhomogeneities, J. Math. Pures Appl. 82 (2003) 749–842.

[5] K. Aydin, A. Hizal, On the completeness of the spherical vector wave functions, J. Math. Anal. Appl. 117 (1986) 428–440.
[6] L. Beilina, M. Cristofol, K. Niinimäki, Optimization approach for the simultaneous reconstruction of the dielectric permittivity and magnetic permeability functions from limited observations, Inverse Probl. Imaging 9 (2015) 1–25.
[7] E.J. Bond, X. Li, S.C. Hagness, B.D. Van Veen, Microwave imaging via space-time beamforming for early detection of breast cancer, IEEE Trans. Antennas Propag. 51 (2003) 1690–1705.
[8] B.M. Brown, M. Marletta, J.M. Reyes, Uniqueness for an inverse problem in electromagnetism with partial data, J. Differ. Equ. 260 (2016) 6525–6547.
[9] F. Cakoni, D. Colton, P. Monk, The Linear Sampling Method in Inverse Electromagnetic Scattering, SIAM, Philadelphia, 2011.
[10] F. Cakoni, D.L. Colton, A Qualitative Approach to Inverse Scattering Theory, vol. 767, Springer, New York, 2014.
[11] P. Caro, On an inverse problem in electromagnetism with local data: stability and uniqueness, Inverse Probl. Imaging 5 (2011) 297.
[12] J. Chen, Z. Chen, G. Huang, Reverse time migration for extended obstacles: electromagnetic waves, Inverse Probl. 29 (2013) 085006.
[13] X. Chen, Computational Methods for Electromagnetic Inverse Scattering, Wiley-IEEE Press, Singapore, 2018.
[14] Y.T. Chow, F. Han, J. Zou, A direct sampling method for simultaneously recovering inhomogeneous inclusions of different nature, SIAM J. Sci. Comput. 43 (2021) A2161–A2189.
[15] Y.T. Chow, K. Ito, K. Liu, J. Zou, Direct sampling method for diffusive optical tomography, SIAM J. Sci. Comput. 37 (2015) A1658–A1684.
[16] Y.T. Chow, K. Ito, J. Zou, A direct sampling method for electrical impedance tomography, Inverse Probl. 30 (2014) 095003.
[17] Y.T. Chow, K. Ito, J. Zou, A time-dependent direct sampling method for recovering moving potentials in a heat equation, SIAM J. Sci. Comput. 40 (2018) A2720–A2748.
[18] Y. Deng, X. Liu, Electromagnetic imaging methods for nondestructive evaluation applications, Sensors 11 (2011) 11774–11808.
[19] S. Gdoura, A. Wahab, D. Lesselier, Electromagnetic time reversal and scattering by a small dielectric inclusion, J. Phys. Conf. Ser. 386 (2012) 012010, IOP Publishing.
[20] K. Ito, B. Jin, J. Zou, A direct sampling method for inverse electromagnetic medium scattering, Inverse Probl. 29 (2013) 095018.
[21] K. Ito, B. Jin, J. Zou, A direct sampling method to an inverse medium scattering problem, Inverse Probl. 28 (2012) 025003.
[22] H.M. Jol, Ground Penetrating Radar Theory and Applications, Elsevier, Amsterdam, 2008.
[23] A. Kirsch, N. Grinberg, The Factorization Method for Inverse Problems, Oxford Lecture Series in Mathematics and Its Applications, vol. 36, Oxford University Press, New York, 2008.
[24] J. Li, J. Zou, A direct sampling method for inverse scattering using far-field data, Inverse Probl. Imaging 7 (2013) 757–775.
[25] K. Liu, Two effective post-filtering strategies for improving direct sampling methods, Appl. Anal. 96 (2017) 502–515.
[26] S.K. Nune, P. Gunda, P.K. Thallapally, Y.-Y. Lin, M. Laird Forrest, C.J. Berkland, Nanoparticles for biomedical imaging, Expert Opin. Drug Deliv. 6 (2009) 1175–1194.
[27] W.-K. Park, Topological derivative strategy for one-step iteration imaging of arbitrary shaped thin, curve-like electromagnetic inclusions, J. Comput. Phys. 231 (2012) 1426–1439.
[28] R. Potthast, A study on orthogonality sampling, Inverse Probl. 26 (2010) 074015.
[29] H. Scharfetter, R. Casañas, J. Rosell, Biological tissue characterization by magnetic induction spectroscopy (mis): requirements and limitations, IEEE Trans. Biomed. Eng. 50 (2003) 870–880.
[30] M. Soumekh, Synthetic Aperture Radar Signal Processing, vol. 7, Wiley, New York, 1999.
[31] C. Tai, I. Antennas, P. Society, I.M. Theory, T. Society, Dyadic Green Functions in Electromagnetic Theory, IEEE Press Series on Electromagnetic Waves, IEEE Press, New York, 1994.
[32] W. Zhang, Q.H. Liu, Three-dimensional scattering and inverse scattering from objects with simultaneous permittivity and permeability contrasts, IEEE Trans. Geosci. Remote Sens. 53 (2014) 429–439.
[33] Y. Zhong, X. Chen, Music imaging and electromagnetic inverse scattering of multiple-scattering small anisotropic spheres, IEEE Trans. Antennas Propag. 55 (2007) 3542–3549.